Poleward Moving Auroral Forms and Dayside Flow Channels

Master's Thesis

submitted by

Anton Goertz

Department of Arctic Geophysics

University Centre of Svalbard

Goethe University Frankfurt

August 2021

Supervisors:

Assoc. Prof. Lisa Baddeley

Prof. Noora Partamies

Prof. René Reifarth

Abstract

Interactions between the magnetosphere and the interplanetary magnetic field (IMF) are not completely understood. At the dayside magnetopause, the IMF and the magnetosphere can reconnect in a pulsed manner, giving rise to a flux transfer event (FTE). Signatures of FTEs can be observed optically, as poleward moving auroral forms (PMAFs) and using radars, as flow channel events (FCEs), in the dayside polar cap ionosphere. It has been suggested that PMAFs may be triggered by other phenomena, such as solar wind pressure pulses (SWPPs). This thesis investigates the driving mechanisms and characteristics of PMAFs using optical data taken at the Kjell Henriksen Observatory in Longyearbyen, Svalbard, OMNI data relating to solar wind and interplanetary magnetic field (IMF) conditions, and HF radar data from Hankasalmi, Finland. Results indicate that PMAFs in this dataset were triggered by FTEs (rather than SWPPs). This is inferred from, 1) observations of decreases in IMF Bz shortly before the start of PMAF events, 2) measurements of comparatively high precipitation energies associated with PMAFs, and 3) the lack of observations of short term solar wind pressure enhancements prior to the occurrence of a PMAF event.

Furthermore, simultaneous optical and radar observation of FTE signatures have been conducted, showing PMAFs tend to occur within localized patches of enhanced flow. The observed flow channels are suspected to be part of a dynamic small scale current system that forms as a consequence of the upward current sheet caused by auroral electron precipitation, as described by Southwood (1987).

Moreover, this thesis presents the first study of the arciness index in relation to dayside aurora. PMAFs manifest themselves as arc-like aurora, suggesting the arciness index could serve to identify PMAFs by distinguishing them from other aurora. It has been

found that while typical arciness values of PMAFs do not significantly differ from the dayside, arciness exhibits a characteristic evolution over the course of a PMAF, which may be used to identify PMAFs.

Contents

List of Abbreviations

AAMLAT	Altitude adjusted magnetic latitude
ASC	All sky camera
ACF	Auto correlation function
BPS	Boundary plasma sheet
CPS	Central plasma sheet
EBI	Equatorward boundary intensification
FAC	Field-aligned current
FCE	Flow channel event
FTE	Flux transfer event
GSM	Geocentric solar magnetospheric coordinate system
IMF	Interplanetary magnetic field
LLBL	Low latitude boundary layer
MHD	Magnetohydrodynamics
MLAT	Magnetic latitude
MLT	Magnetic local time
MSP	Meridian scanning photometer
OCB	Open-closed boundary
PMAF	Poleward moving auroral form
PMRAF	Poleward moving radar auroral form
PSBL	Plasma sheet boundary layer
SPEA	Superposed epoch analysis
SWPP	Solar wind pressure pulses
SuperDARN	Super Dual Auroral Radar Network
UT	Universal time

1 Introduction

The magnetosphere shields the Earth from the fast moving charged particles emitted by the sun, called the solar wind, and protects all life and technology within it. The solar wind and the interplanetary magnetic field (IMF) constantly interact with the magnetosphere. The dynamics of that interaction are heavily influenced by the conditions of the solar wind and the orientation of the IMF. At the border between the IMF and the dayside magnetosphere, the so called magnetopause, magnetic field lines from both domains merge and form new magnetic field lines, that directly connect the magnetosphere to interplanetary space, in a process known as magnetic reconnection. This reconnection is typically not steady, as previously thought, but often occurs in a pulsed and sporadic fashion. Each reconnection event is called a flux transfer event (FTE), named after the transport of magnetic flux as well as solar wind particles from interplanetary space into the magnetosphere. Electrons in this plasma are heated and can precipitate into the polar cap ionosphere, depositing their energy by colliding with atmospheric particles, rendering them ionized or excited. These particles can then emit light with characteristic wavelengths and colours, green and red in the case of oxygen atoms, giving rise to aurora.

During magnetic reconnection, as in FTEs, magnetic field lines transition from being closed, meaning they form a closed loop within the magnetosphere, to being open, implying magnetospheric field lines connect to the IMF. As the solar wind travels past the Earth, one end of the open field lines is being carried with it. Consequently, the foot of each field line, which is located in the polar ionosphere, is dragged anti-sunward across

the polar cap. Hence, the location in the ionosphere at which particles on these field lines precipitate moves anti-sunward as well. This gives rise to an auroral form, which forms in the dayside ionosphere and moves poleward, a poleward moving auroral form (PMAF). Thus, PMAFs are believed to be the ionospheric signature of FTEs (Sandholt 1986). However, there have been reports of other phenomena, mainly short term enhancements in the pressure of the solar wind (solar wind pressure pulses, SWPPs), as a trigger for PMAFs. One goal of this project was to find large numbers of PMAFs occurring over many years (a random sample) and determine their trigger mechanism, in order to understand PMAF formation rate due to FTEs and SWPPs.

Furthermore, this project will utilize arciness, an index quantifying how arc-like auroral structures appear, first introduced by Partamies et al. (2014). Arciness was found to be not only closely related to the occurrence of auroral arcs, but also a reliable and objective assessment of auroral morphology. In this project, the behaviour of arciness on the dayside is studied for the first time. Additionally, PMAFs manifest themselves as arcs in all sky camera (ASC) images, suggesting arciness could enable identification of PMAFs.

The last major question this project seeks to address is related to dayside flow channels. Flow channel events (FCEs) are the ionospheric signature of FTEs as observed by radars. They manifest themselves as latitudinally aligned channels of enhanced ionospheric flow. Southwood (1987) originally described FTEs and how their ionospheric signature, including these channels, would appear. He predicted the existence of a small scale dynamic current system, consisting of an upward current caused by electron precipitation, that is connected to a downward current by a FCE. Southwood concluded, there would be a central anti-solar flow associated with the an ionospheric signature of a FTE. This project aims to combine optical measurements of PMAFs with radar data in order to observe this flow.

2 Theoretical Background

This chapter introduces a surface-level space physics background covering the solar wind and the interplanetary magnetic field, the magnetosphere and ionosphere, as well as basic auroral dynamics. All material covered in this chapter is based on Baumjohann and Treumann's '*Basic Space Plasma Physics*' (2012) and Brekke's *'Physics of the Upper Polar Atmosphere'* (2013), unless otherwise indicated.

2.1 Single Particle Motion

In order to understand the dynamics of ionospheric and magnetospheric plasma it is useful to consider the behaviour of individual particles in the presence of electromagnetic fields. The fundamental equation governing that behaviour is the Lorentz equation:

$$\vec{F} = q\left(\vec{E} + \vec{v} \times \vec{B}\right) \tag{1}$$

which describes the relationship between the electromagnetic force $\vec{F}$ acting on a particle of charge q and velocity $\vec{v}$ and the encompassing electric and magnetic fields $\vec{E}$ and $\vec{B}$, respectively.

In the presence of a homogeneous magnetic field and a vanishing electric field $\vec{E} = 0$, particles experience a force perpendicular to their direction of motion causing them to engage in circular motion around the magnetic field line, where the direction of rotation depends on the charge of the particle. This motion is referred to as gyration. As there

is no force parallel to the magnetic field line, particles can move in that direction with constant velocity. Combined, this motion leads to a corkscrew-like trajectory (for $\vec{v}_{\parallel} \neq 0$).

The radius r_g and frequency ω_g of gyration depend on the magnetic field strength, the particles' specific charge q/m and the component of their velocity, that is perpendicular to the magnetic field $v_{\perp}$:

$$\omega_g = \frac{qB}{m} \qquad\qquad r_g = \frac{mv_{\perp}}{qB} \tag{2}$$

Gyration is the basis of all motion of plasma in interplanetary space, the magnetosphere and the ionosphere. Frequently, that motion is disturbed by either the presence of an electric field or inhomogeneities in the magnetic field that manifest themselves as gradients or field line curvature, all of which lead to an underlying drift motion. Several types of drifts will be explained hereinafter.

General Force Drift

It can be shown that any arbitrary force $\vec{F}$ acting on a gyrating particle will cause a drift with velocity $\vec{v}_F$:

$$\vec{v}_F = \frac{1}{qB^2}\left(\vec{F} \times \vec{B}\right) \tag{3}$$

There are a number of drifts that can be described using the general force drift equation.

$E \times B$ - Drift

When taking into account an electric field that may be present, typically one only has to consider the component perpendicular to the magnetic field, as any parallel component would quickly be cancelled out by electrons freely moving along magnetic field lines. Inserting the Coulomb force $\vec{F} = q\vec{E}$ into equation (3) yields:

$$\vec{v}_D = \frac{\vec{E} \times \vec{B}}{B^2} \tag{4}$$

The direction of this drift, commonly referred to as $E \times B$ - drift, is perpendicular to both the electric and magnetic field. The $E \times B$ - drift can be interpreted as the consequence of the change of the radius of curvature due to the resulting electromagnetic force. This force has two components, the Coulomb force, which always acts in the same direction, and the Lorentz force, which acts perpendicular to the direction of motion. The interplay of those two forces can decrease the radius of curvature, when both forces act in the same direction, and increase the gyration radius, when both forces act in opposing directions. As a consequence, after one gyroperiod charged particles have drifted away from their original position.

It is also interesting to note, that the drift velocity is independent of the plasma particles' properties, such as mass and charge, meaning the $E \times B$ - drift by itself can not give rise to electric currents, as ions and electrons both drift in the same direction at the same rate. The Coulomb force is the only force that doesn't produce an electric current when acting on charged particles in a magnetic field, since its direction depends on the charge of the particle. All other forces do not depend on the electric charge of the particle they act on, causing them to create an electric current, as the direction of the drift they produce does depend on the electric charge (equation 1).

The general force equation can also be used to determine the drift velocity due to the curvature of a magnetic field line.

Curvature Drift

In this case the force acting on a particle gyrating along a curved magnetic field line with the radius of curvature R_c is given by the centripetal force $\vec{F}_c = \frac{mv^2}{R_c}$, which ultimately gives rise to a curvature drift $\vec{v}_c$:

$$\vec{v}_c = \frac{mv_{\parallel}^2}{qR_c^2B^2}\left(\vec{R}_c \times \vec{B}\right) \tag{5}$$

Curvature drift is partly responsible for the ring current in the magnetosphere (chapter 2.5), causing ions to drift westward and electrons to drift eastward. The other cause of the ring current is gradient drift.

Gradient Drift

In an environment where the magnetic field strength is not constant, it is only the component of the gradient that is perpendicular to the magnetic field itself that contributes to drift motion. As particles gyrate, they move in a plane that includes the perpendicular component of the gradient of the magnetic field. Consequently, the gyro radius is not constant, but changes throughout the particles' orbits, due to its dependence on the magnetic field strength (equation 2). This gives rise to a net drift in a direction perpendicular to both the magnetic field and its gradient. Since ions and electrons gyrate in opposite directions due to their different charges, their drift directions are opposite as well. Additionally, the different masses of electrons and ions lead to significant differences in drift velocity. The gradient drift velocity $\vec{v}_\nabla$ can be expressed as:

$$\vec{v}_\nabla = \frac{mv_{\perp}^2}{2qB^3}\left(\vec{B} \times \vec{\nabla}B\right) \tag{6}$$

Due to the cross product between the magnetic field and its gradient field, only the component of the gradient field perpendicular to the magnetic field contributes to the drift, as previously mentioned. Any parallel component will also cause the gyration radius to change, however this will not lead to any drift motion. Instead, as charged particles move parallel to the magnetic field (and its gradient), the field strength increases causing the parallel velocity of the particles to decrease. This is due to the

conservation of the magnetic moment (or 'first adiabatic invariant') μ:

$$\mu = \frac{mv_{\perp}^2}{2B} \tag{7}$$

If the magnetic field strength increases to a critical point, then the parallel velocity goes to zero and particles are reflected in a process known as magnetic mirroring. Whether or not a given particle will be reflected by magnetic mirroring is determine by the so called loss cone. Particles with pitch angles (relative to the magnetic field) in the loss cone precipitate into the ionosphere, while those outside the loss cone are reflected. This can cause charged particles to be trapped on closed magnetic field lines, as is the case for all particles that make up the Van Allan radiation belts. Particles in the Van Allan belts continually gyrate around magnetic field lines and engage in gradient and curvature drift. Additionally, those particles bounce between hemispheres as a consequence of magnetic mirroring. These mirroring points can lie within the ionosphere, which enables such particles to cause auroral emissions.

Figure 2.1 gives an overview of relevant drifts and their associated ion and electron trajectories. As can be seen, in all cases with the exception of $E \times B$ - drift, ions and electrons drift in opposite directions, leading to the flow of currents associated with each of the drifts.

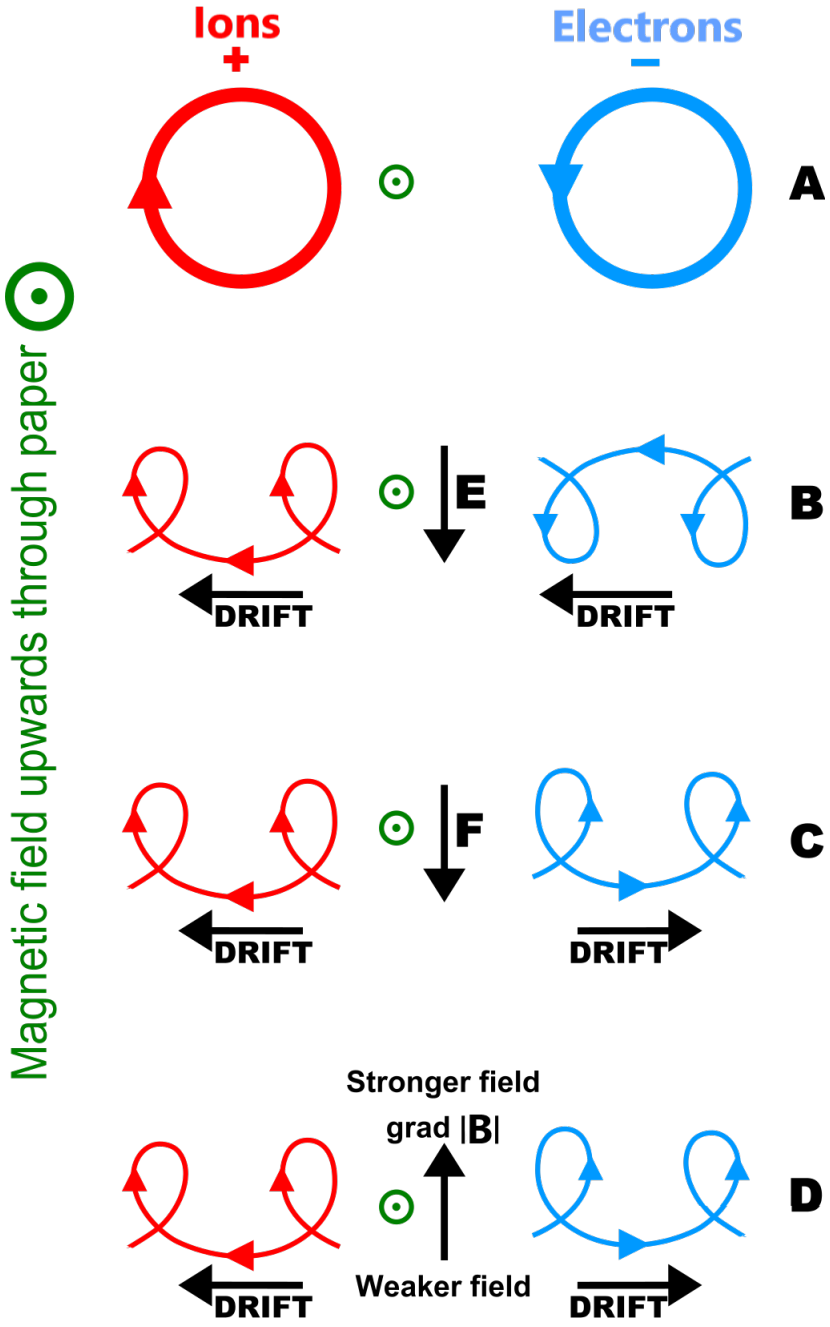

Figure 2.1: Electron and ion trajectories under the influence of different electric and magnetic field configurations: homogeneous B-field and no electric field (A), perpendicular and homogeneous E and B fields (B), arbitrary force independent of the sign of the electric charge on particles in a homogeneous B-field (C) and inhomogeneous magnetic field (D). Figure adapted from Wikimedia commons.

2.2 Solar Wind

The solar atmosphere is comprised of three distinct layers: the photosphere, the chromosphere and the corona. Temperatures in the corona are very high and can exceed 10^6 K, which enables coronal electrons to reach escape velocity. While ions in the corona generally have insufficient thermal energies to escape the sun's gravity, they are dragged along by electrons and escape into space. These particles comprise what is known as the solar wind. While solar wind plasma consists mainly of electrons and protons, α-particles (He^{++}) make up approximately 4% of the plasma.

The solar wind particles move radially outward from the sun in an omni-directional manner, causing the particle density to decrease with the square of the distance to the sun. The behaviour of the solar wind plasma is governed by three physical quantities: solar wind speed, particle density and electron temperature. Typical values for those quantities are listed in table 2.1. It is worth mentioning, that the properties of the solar wind are not constant, but can change over short time frames (in a matter of minutes). Thus, the values for each physical quantity listed in table 2.1 are averages, while specific values at any given time may differ by approximately one order of magnitude.

The solar wind also plays an important role for the magnetic field in our solar system, the interplanetary magnetic field (IMF). Due to the near infinite conductivity of space plasmas, charged particles in the solar wind carry the sun's magnetic field with them, as they escape the corona. This condition, commonly referred to as the 'frozen-in' condition, will be explored in more detail hereinafter.

Speed	Particle Density	Electron Temperature
500 km/s	$5\,\mathrm{cm}^{-3}$	10^5 K

Table 2.1: Median values for various physical quantities of solar wind plasma as observed by multiple spacecraft at approximately 1 AU distance to the sun [Baumjohann and Treumann, 2012].

2.3 Alfvén's Theorem

The 'frozen-in' condition, also known as Alfvén's theorem, can be shown using Ohm's law in the case of near-infinite conductivity $\sigma \to \infty$:

$$\frac{\vec{j}}{\sigma} = \vec{E} + \vec{v} \times \vec{B} \to 0 \implies \vec{E} = -\vec{v} \times \vec{B} \tag{8}$$

where $\vec{j}$, $\vec{E}$ and $\vec{B}$ represent the current density, electric field and magnetic field, respectively. Inserting this relation into Faraday's law yields:

$$\frac{\partial \vec{B}}{\partial t} = -\vec{\nabla} \times \vec{E} = \vec{\nabla} \times \left(\vec{v} \times \vec{B}\right) \tag{9}$$

First, we consider a surface S with a perimeter L that is moving with velocity $\vec{v}$. The time derivate of the magnetic flux, Φ, through that surface can be expressed in terms of the change in the magnetic field (first term) and the motion of the surface (second term):

$$\frac{d\Phi}{dt} = \iint_S \frac{\partial \vec{B}}{\partial t} d\vec{S} + \oint_L \vec{B} \cdot (\vec{v} \times d\vec{l}) \tag{10}$$

Rearranging the second term and applying Stokes theorem yields:

$$\frac{d\Phi}{dt} = \iint_S \frac{\partial \vec{B}}{\partial t} d\vec{S} - \oint_L (\vec{v} \times \vec{B}) \cdot d\vec{l}, \qquad \oint_L (\vec{v} \times \vec{B}) \cdot d\vec{l} = \iint_S \vec{\nabla} \times (\vec{v} \times \vec{B}) \cdot d\vec{S} \tag{11}$$

Finally, inserting Faraday's law into the second term will show, that magnetic flux is conserved:

$$\frac{d\Phi}{dt} = \iint_S \frac{\partial \vec{B}}{\partial t} d\vec{S} - \iint_S \vec{\nabla} \times (\vec{v} \times \vec{B}) \cdot d\vec{S} = \iint_S \left[\frac{\partial \vec{B}}{\partial t} - \vec{\nabla} \times (\vec{v} \times \vec{B})\right] \cdot d\vec{S} = 0 \tag{12}$$

Consequently, the magnetic field is frozen into the plasma. This means, that plasma can be considered a fluid which drags along the magnetic field lines.

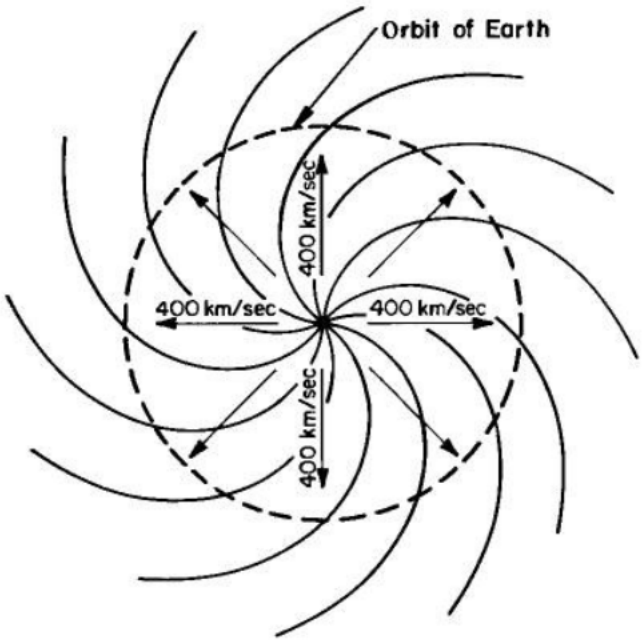

Figure 2.2: Interplanetary magnetic field lines in the shape of an Archimedean spiral [Kivelson and Russel, 1995].

2.4 Interplanetary Magnetic Field

As the solar wind plasma escapes the corona, it carries the coronal magnetic field with it, which gradually becomes the IMF. The foot of the IMF field line always remains in the corona, which rotates along with the sun, causing the IMF lines to assume a spiral shape (Parker spiral) as shown in figure 2.2.

The IMF strength is not inversely proportional to the cube of the distance to the sun, ($B \propto 1/r^3$), as would be the case for a simple magnetic dipole. Instead, due to the spiral shape, there are different dependencies for the radial and azimuthal components ($B_r \propto 1/r^2$ and $B_\varphi \propto 1/r$), yet the total strength of the IMF is still greater than would be expected for a dipole field. This dichotomy is explained by the solar wind plasma

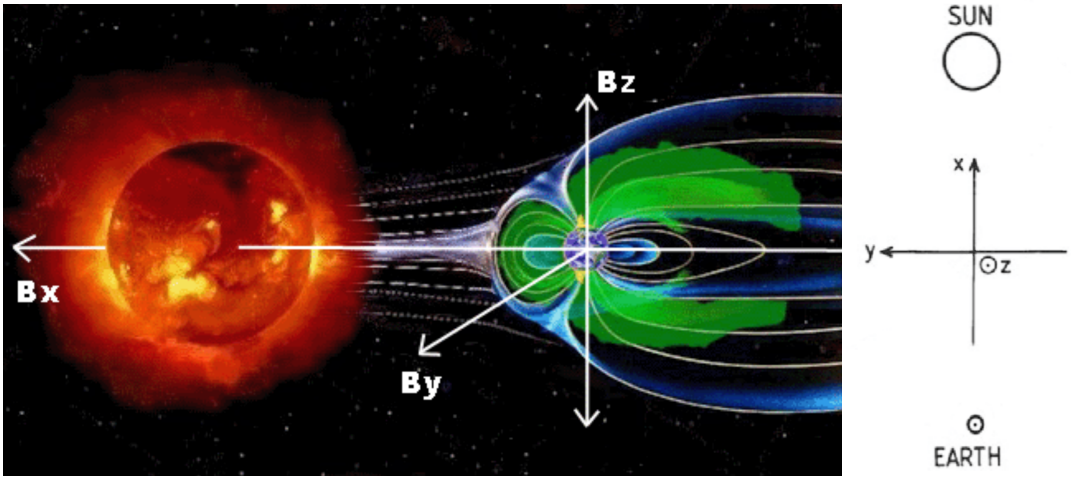

Figure 2.3: Illustration of the geocentric solar magnetospheric coordinate system [SpaceWeatherLive, 2021].

moving through interplanetary space, inducing electric currents, which induce magnetic fields that enhance the original field, as described by magnetohydrodynamics (MHD). This magnetic dynamo effect causes the field strength at 1 AU to be about 100 times stronger. The IMF strength at 1 AU ranges from roughly 3 to 12 nT and can change quickly, just as the orientation of the IMF does.

In order to describe the IMF, the geocentric solar magnetospheric coordinate system (GSM) is most appropriate. This coordinate system is illustrated in figure 2.3. The origin of the coordinate system is placed in Earth's centre. The x-direction is oriented towards the centre of the sun, while the y-direction is perpendicular to both the x-direction and the Earth's dipole axis and pointing towards dusk. The z-direction is defined as the direction that is perpendicular to both the x and y-axis, which is *not* necessarily along Earth's dipole axis [Laundal, 2017].

2.5 Magnetosphere

Convection currents in the Earth's outer core and mantle are responsible for the creation of approximately 95% of Earth's magnetic field. There are other sources that contribute to Earth's magnetic field, such as electromagnetically induced fields in the ionosphere and magnetosphere as well as crustal fields. The typical magnetic field near the poles is approximately twice as strong as at the equator ($B_{\text{pol}} = 60\,\mu\text{T}$, $B_{\text{eq}} = 30\,\mu\text{T}$).

Earth's magnetic field can be modelled as a dipole field at close distances (within a few R_E) whose axis deviates by about 11° from the rotation axis. The actual shape of the magnetosphere is heavily influenced by the solar wind. The frozen-in solar wind plasma exerts pressure on the dayside magnetosphere, causing it to compress significantly. Inversely, the nightside magnetosphere (the magnetotail) is elongated to a substantial degree due to solar wind interactions, as depicted in figure 2.4.

The solar wind particles are supersonic in interplanetary space. Upon approaching Earth's magnetosphere most of them are deflected around it, whereas some are decelerated to subsonic speeds. This creates a sunward shock wave called the bow shock. In the process of slowing down the solar wind particles, most of their kinetic energy is converted into thermal energy, heating the plasma. The region between bow shock and the magnetosphere is known as the magnetosheath. Magnetosheath plasma has higher density and temperature compared to solar wind plasma causing the magnetic field strength to increase as well.

The boundary between the Earth's magnetic field and the magnetosheath is called the magnetopause. Depending on the solar wind conditions, the distance between the dayside magnetopause and the Earth can range from 6 to 15 R_E. The dayside magnetopause acts as a protective shield deflecting charged particles around it. As charged particles reach the magnetopause, the ambient magnetic field strength increases suddenly and significantly. This causes ions to move eastwards and electrons to move westwards be-

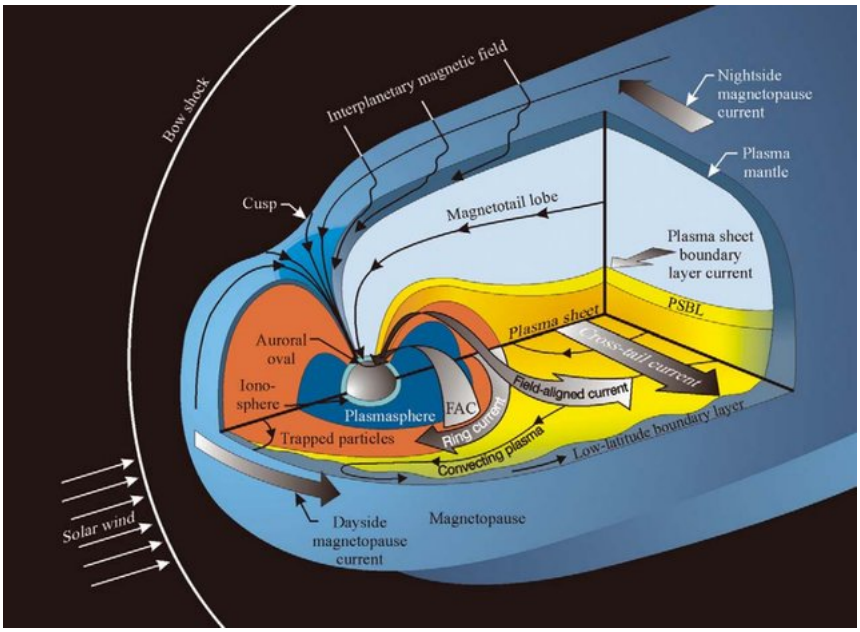

Figure 2.4: Schematic diagram portraying the structure of Earth's magnetosphere. Figure from Pollock et al. (2003).

fore being deflected back into the magnetosheath, giving rise to an eastward current along the magnetopause. This current is conveniently named the dayside magnetopause current, or Chapman-Ferraro current (see fig. 2.4).

The magnetosphere can be divided up further on the basis of how plasma is distributed in it, in which case one ends up with four different constituents: The radiation belts, the plasma sheet, the plasma sphere and the lobe. The radiation belts (Van Allen belts) contain very high energy particles that are trapped on closed field lines by magnetic mirroring (chapter 2.1). The Van Allen belts are also home to particles that make up the ring current, which is created by the westward drift of ions (and eastward drift of electrons) due to gradient and curvature drift. The plasmasphere is engulfed by the Van Allen belts and can be considered a torus shaped extension of the ionosphere containing cool plasma.

The plasma sheet contains most of the hot magnetotail plasma and extends out far into the nightside magnetosphere. It is surrounded by the magnetotail lobe, which contains

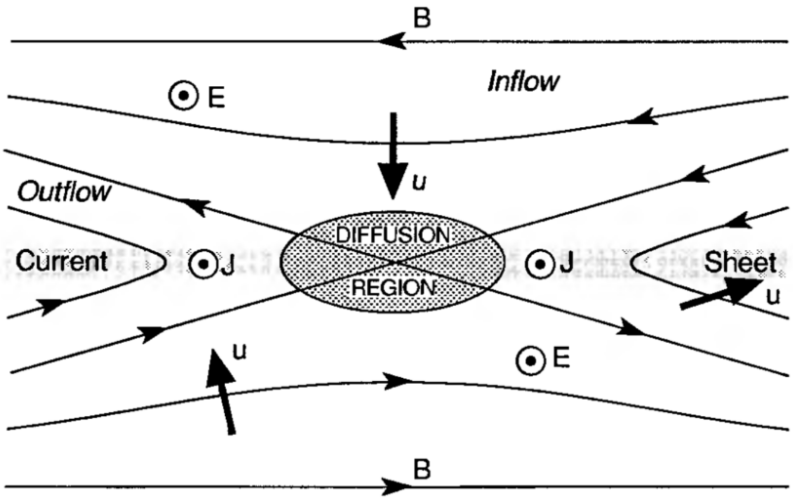

Figure 2.5: Topology of magnetic field lines during reconnection [Kivelson and Russel, 1995].

cool plasma. The lobe and plasma sheet are separated by the plasma sheet boundary layer (PSBL). The plasma sheet contains a neutral current sheet located in the region, where magnetic field lines oriented away from Earth (from the southern hemisphere) and towards Earth (northern hemisphere) meet. This current can be understood by applying Ampère's law across the boundary between two oppositely directed field lines (see section 2.5.1). Together with the magnetopause current, which flows dusk to dawn along in the magnetotail, the neutral current sheet forms a current system often referred to as the θ-current, due to the resemblance of its shape with the Greek letter.

2.5.1 Magnetic Reconnection

As previously mentioned, the magnetosphere acts as a protective shield by deflecting charged solar wind particles. This can be understood by considering the frozen-in approximation, which prevents solar wind plasma from mixing with magnetospheric plasma, as they are each frozen into their respective magnetic fields. However, the frozen-in approximation breaks down when the magnetic fields carried by two plasmas

that are approaching one another is antiparallel. This configuration is present at the dayside magnetopause during southward IMF. As the plasmas approach each other, a strong current sheet is formed at the boundary layer. This is a consequence of Ampere's law for static electric fields:

$$\oint \vec{B} \cdot d\vec{s} = \mu_0 I_{\text{enlosed}} \tag{13}$$

where I_{enclosed} refers to the current flowing through the surface enclosed by the path $\vec{s}$. The opposing fields increase in strength and give rise to a current sheet that also has to increase in strength to satisfy Ampere's law. When the plasmas with near infinite conductivity can no longer create a strong enough current, a magnetic quadrupole forms and the magnetic field lines from both domains merge. This process is known as magnetic reconnection. Figure 2.5 shows the magnetic field configuration after the creation of the magnetic quadrupole, along with the sheet current.

This process allows plasma to transfer across from one domain to the other inside the diffusive region (see fig. 2.5), whereby magnetic potential energy is converted into thermal and kinetic energy, heating and accelerating the plasma. The magnetic quadrupole then disappears and the magnetic field lines have a new configuration, in which each field line crosses both domains.

Magnetic reconnection remains poorly understood and is a very active area of research. Understanding when and where it occurs in the magnetosphere is very relevant for auroral physics, as reconnection offers a way for solar wind plasma to enter the magnetosphere.

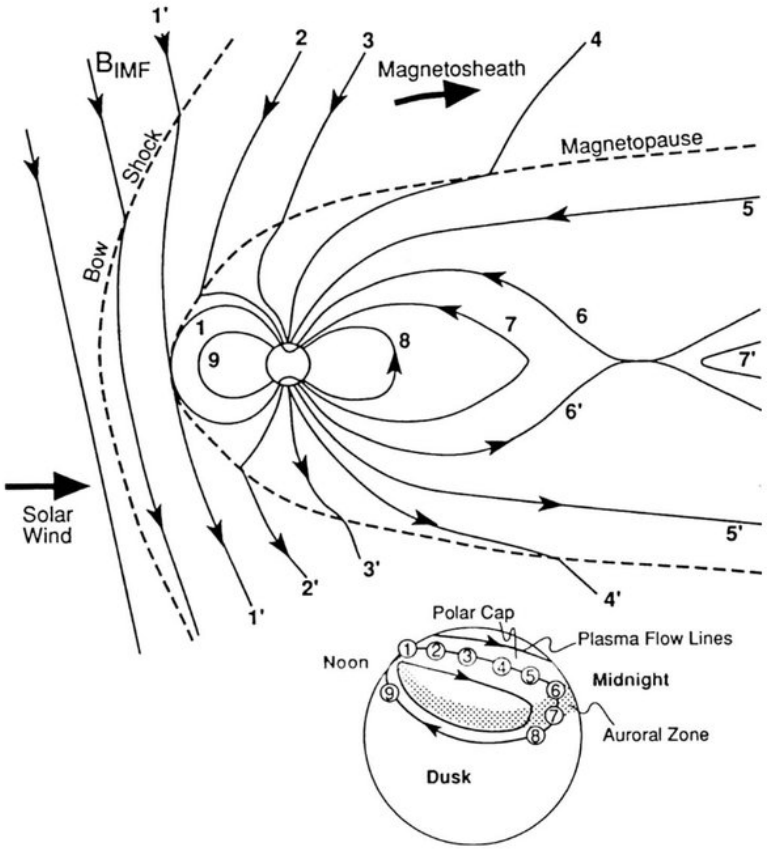

Figure 2.6: Schematic diagram showing different steps of the Dungey cycle [Kivelson and Russel, 1995].

2.5.2 Dungey Cycle

Magnetic reconnection between the magnetosphere and the IMF occurs at two places: at the dayside magnetopause (dayside reconnection) and in the magnetotail (nightside reconnection). Due to magnetic reconnection taking place continuously, the topology of the magnetosphere and the IMF changes constantly. The Dungey cycle, named after J. W. Dungey, describes how magnetospheric field lines reconnect to the IMF and move by convection.

Figure 2.6 shows nine different time steps in the Dungey cycle starting at the dayside

reconnection point. The geomagnetic field line at $t = 1$ in figure 2.6 depicts a closed field line in the magnetosphere that is reconnecting to the IMF field line marked as 1'. During dayside reconnection, solar wind plasma can enter the magnetosphere and travel along the open magnetic field line into the ionosphere to create auroral emissions. In this context, open field lines are geomagnetic field lines that have reconnected to the IMF. A closed field line is a field line, that forms a closed loop inside the magnetosphere. The boundary between open and closed field lines in the ionosphere is referred to as the open-closed-boundary (OCB). In the case of figure 2.6, the OCB lies slightly equatorward of where field line at $t = 1$ meets the ionosphere.

Time steps 2 through 5 (as well as 2' through 5') show open field lines convecting towards the magnetotail. In this process, as the solar wind plasma travels past Earth, it carries with it one end of the open field line. The foot of each field line (located in the ionosphere) is thus dragged anti-sunward across the polar cap. This motion manifests itself as an induced $E \times B$ drift of ionospheric plasma (see eq. 4). The polar cap is defined as the area in the polar ionosphere enclosed by the OCB.

At $t = 6$, one open magnetic field line in the northern hemisphere reconnects with another from the southern hemisphere in the magnetotail. During magnetotail reconnection, solar wind plasma is transferred into the plasma sheet and accelerated along magnetic field lines into the ionosphere, which can ultimately lead to the formation of nightside aurora. Throughout time steps 7, 8 and 9, closed field lines and ionospheric plasma are convecting from midnight towards noon over the dawn and dusk sectors to complete the cycle. In combination with time steps 2 to 5, this leads to the formation of two polar ionospheric convection cells. Typical convection speeds in the ionospheric convection pattern lie around several hundreds of meters per second.

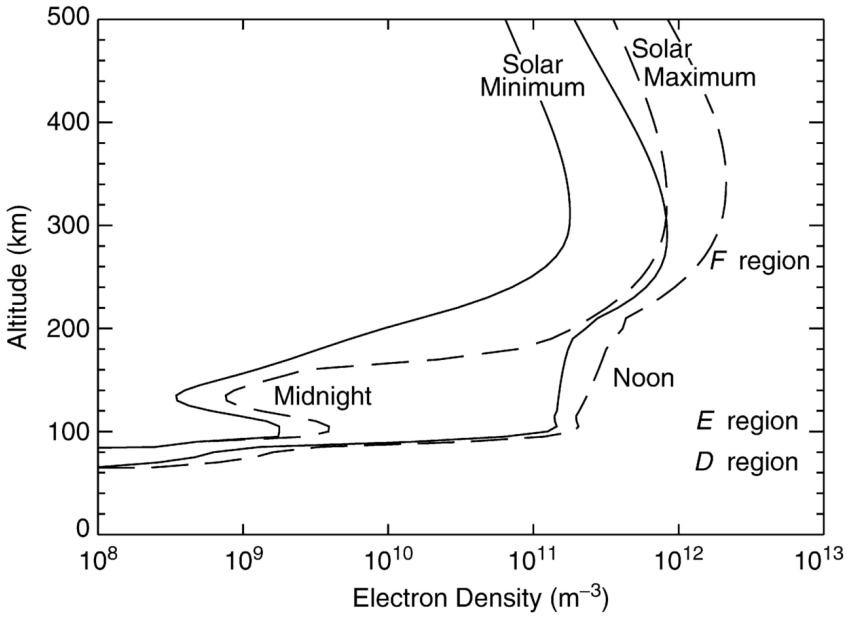

Figure 2.6: Electron density profile of the ionosphere for different local times and solar activities. [Kivelson and Russel, 1995].

2.6 Ionosphere

The ionosphere is a weakly ionized plasma that is part of the terrestrial atmosphere spanning several different layers from approximately 90 km (mesosphere) to 1000 km (exosphere) in altitude. It is created primarily by solar ultraviolet and X-rays as well as energetic particle precipitation ionising the neutral atmosphere. Due to the dependence on solar irradiation, the dayside ionosphere is more ionized than the nightside ionosphere, as portrayed in figure 2.6, which shows the electron density as a function of altitude. High solar activity leads to significant increases in solar UV emission [Floyd, 2002], causing higher ionospheric ionisation rates across all altitudes. Generally, the electron density profile has two peaks, the lower one at around 100 km, and a higher one at roughly 250 km altitude. These peaks are the basis for how the ionosphere is divided up into regions. The E and F regions correspond to the lower and higher peak

in the electron density profile, respectively. There is another region called the D region, which is located below the E region.

The D region does not only have the lowest electron densities, it is also the region with the lowest degree of ionization. This is due to high recombination rates of ionized particles, which is a consequence of the high ion-neutral collision frequency that comes along with high atmospheric densities. Another implication of high collision frequencies is that they do not allow for photoemission by excited ions, preventing aurora to form (ch. 2.7). Ionization of nitric oxide by solar hydrogen alpha radiation and complex chemistry determine the dynamics of the D region.

In the E region the primary ionisation mechanism is solar irradiation, in particular soft x-ray and far ultraviolet radiation. Hence, there is a very profound day-night difference between the electron density of approximately three orders of magnitude. The plasma is mainly comprised of nitric oxide and molecular oxygen, with atomic oxygen being the third most abundant ion species. Most auroral emissions originate in the E region, namely the green atomic oxygen line and the blue molecular nitrogen line (see ch. 2.7).

The F region experiences little daily variability, which is a consequence of low recombination rates resulting from low ion-neutral collision frequencies. However, occasionally a secondary peak in the electron density profile (labelled F1) can emerge on the dayside just below the main peak (labelled F2). Atomic oxygen is by far the most abundant ion species in the F region, however lighter ion species such as hydrogen and helium become relevant in the upper part of the F region (topside ionosphere). Electron densities reach a maximum in the F region as the plasma becomes more ionized at high altitudes. The topside ionosphere gradually merges into the plasma sphere.

In order to understand the behaviour of high density plasmas in the presence of electric and magnetic fields, such as the ionosphere, one has to consider all factors influencing the motion of plasma particles. These factors are the Coulomb and Lorentz force as well

as collisions with other particles. In most cases, it is either electromagnetic interactions or collisions that determine the trajectory of a particle. To distinguish between those cases, it is instructive to consider the mobility coefficient k_j for a particle j. It is defined as the gyration period ω_g divided by the collision frequency ν:

$$k_j = \frac{\omega_{g,j}}{\nu_j} = \frac{q_j B}{\nu_j m_j} \tag{14}$$

High values of k_j indicate that the motion of particles will be dominated by electromagnetic interactions (gyration and drifts, see ch. 2.1), as particles will have completed a large number of gyro-orbits prior to colliding with another particle. Inversely, low values of k_j will lead to ions and electrons behaving more like a neutral gas, as their motion is mostly determined by collisions.

In the ionosphere, all parameters in eq. 14 are approximately constant for a given particle, with the exception of the collision frequency. Thus, the mobility coefficient can be approximated as $k_j \propto \frac{1}{\nu_j}$, although it is important to note, that the proportionality factor (the gyration frequency) depends on the particle j. Depending on the ion species, the electron gyration frequency $\omega_{g,e}$ is approximately four orders of magnitude larger than the ion gyration frequency $\omega_{g,i}$.

Figure 2.7 shows the velocity vectors for ions and electrons at different altitudes in the ionosphere. The electron mobility coefficient is large above approximately 75 km altitude, causing them to engage in $E \times B$ - drift. Ions, on the other hand, have low mobility coefficients in the D region and high values of k_i in the F region. In the E region, the value of k_i is around unity.

Since the value for the electron mobility coefficient tends to be higher than the ion mobility coefficient, electrons and ions move in different directions and different rates. This leads to the flow of a current $\vec{j}$:

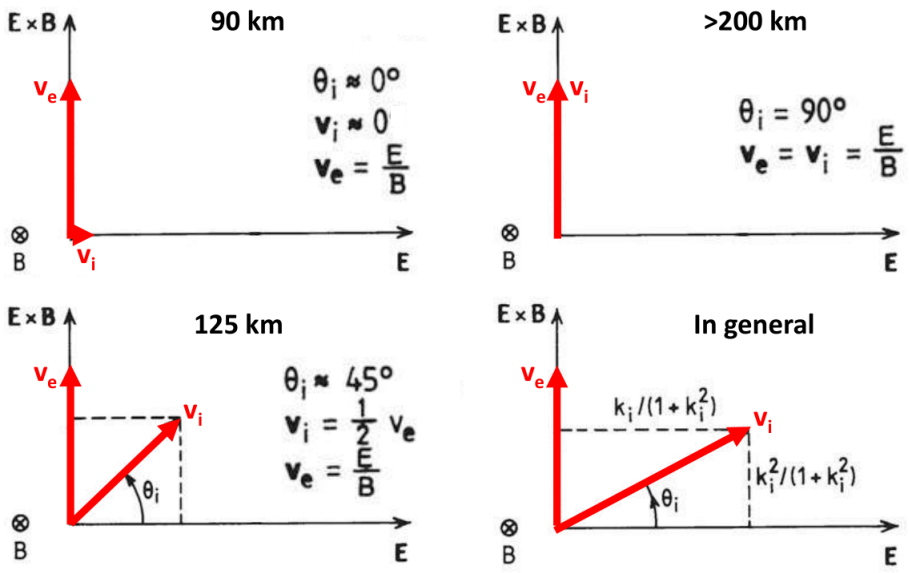

Figure 2.7: Ionic and electronic drift velocities for different altitudes in terms of mobility coefficients.

$$\vec{j} = n_i q_i \vec{v}_i - n_e e \vec{v}_e \tag{15}$$

Where n_i and n_e are the ion and electron densities, respectively. As plasmas are quasi neutral ($n_e = n_i = n$) and if we assume ions to be singly ionized ($q_i = e$), the current density can be written as:

$$\vec{j} = ne(\vec{v}_i - \vec{v}_e) \tag{16}$$

2.6.1 Currents

Currents in ionospheric physics are generally expressed in terms of their components along the electric and magnetic field, and perpendicular to both fields. A current flowing perpendicular to magnetic field lines is referred to as a Pedersen current, while currents along the magnetic field are called Birkeland-, or simply field-aligned currents.

Finally, Hall currents are currents that flow in the direction perpendicular to both the electric and magnetic field.

As can be deduced from figure 2.7, in the lower E region there are Hall currents being generated by the differential motion of ions and electrons. Electrons engage in $E \times B$ - drift, while ion motion is dominated by collisions. With increasing altitude, the Hall component of the current starts to decrease as ion-neutral collisions become sufficiently infrequent for ions to complete full gyro-orbits and to start drifting too. However, collisions still influence ion motion to a substantial degree, frequently disturbing gyrating ions mid-orbit, creating a net ion drift along the electric field, which produces a Pedersen current.

Near 200 km altitude, ions are moving at almost the same velocity as electrons and above 200 km, no significant Hall or Pedersen current can arise. The region of the ionosphere in which currents can be created by this mechanism (80-200 km) is sometimes referred to as the dynamo layer.

An example of a current caused in this manner is the auroral electrojet, located in the auroral oval (see ch. 2.7.1). Electrojets are hall currents and occur at approximately 100 to 150 km in altitude. There are two auroral electrojets in each hemisphere, one flowing from noon to midnight via the dusk sector (eastward electrojet) and one via the dawn sector (westward electrojet). They are connected to the Birkeland currents R1 and R2, coupling the ionosphere to the magnetosphere.

The total current density can be expressed in terms of the Pedersen-, Birkeland- and Hall components:

$$\vec{j} = \sigma_p \vec{E}_\perp - \sigma_h \frac{\vec{E} \times \vec{B}}{B} + \sigma_\parallel \vec{E}_\parallel \tag{17}$$

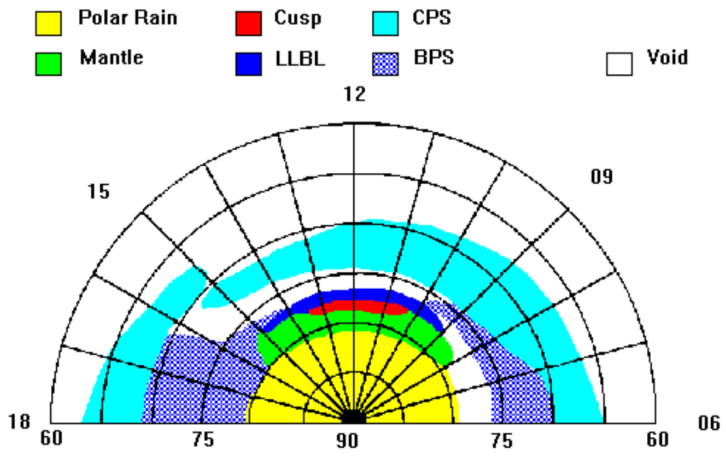

Figure 2.8: Dayside particle precipitation regions colour coded by magnetospheric source regions [Newell and Meng, 1992].

2.6.2 Particle precipitation

As magnetospheric plasma is frozen into the magnetic field, particles on both closed and open field lines can enter the ionosphere. This is referred to as particle precipitation. The intensity and energy of the precipitating particles is determined by the source region. Figure 2.8 gives an overview of where the different regions of the magnetosphere (closed field lines) and the solar wind (open field lines) magnetically map to in the dayside ionosphere. A polar plot of the high latitude regions with the geomagnetic pole in the centre, magnetic latitude on the radial axis and magnetic local time (MLT) on the azimuthal axis is shown. MLT measures time relative to the Earth's magnetic dipole axis, rather than its rotation axis.

The central plasma sheet (CPS, see section 2.5) and its boundary region (BPS) are responsible for mid to low latitude electron precipitation. Since the plasma sheet is concentrated in the magnetotail, precipitation intensities are much higher on the nightside. Electron temperatures in the plasma sheet are comparatively high, which leads

to high precipitation energies (1-20 keV).

The low latitude boundary layer (LLBL) corresponds to the precipitation region in which particles originate from the magnetopause, where magnetospheric and magnetosheath plasma coexist. Typical precipitation energies from the LLBL are around and below 1 keV. The cusp, mantle and LLBL are centred around magnetic noon, however, their exact location depends on the IMF [Sanchez, 1990]. Additionally, the act of opening magnetic field lines on the dayside and closing them on the nightside causes the entire polar cap to expand and contract in latitude. The mantle and cusp region have similar precipitation energies to the LLBL, while LLBL and mantle precipitation is comprised exclusively of electrons, unlike the cusp, where protons also precipitate. Precipitation in the cusp originates from open field lines that just reconnected, allowing solar wind plasma direct access to the ionosphere. The study presented in this thesis focusses on cusp aurora.

2.7 Aurora

Aurora (also known as the polar, northern or southern lights) is a natural phenomenon in the polar ionosphere in which typically green or red light can be observed in the night sky. Aurora in the northern hemisphere is called Aurora Borealis, while in the southern hemisphere it is called Aurora Australis. It can manifest itself in different shapes, such as diffuse aurora, auroral arcs, patches or rays. Aurora can form on any planet with a magnetosphere and an atmosphere, and has been observed on Earth, Mars and all gas giants in the solar system [Sandel, 1981, Bertaux, 2005].

Solar wind plasma can enter the magnetosphere via open field lines and magnetic reconnection. It can directly precipitate into the polar ionosphere along newly reconnected open magnetic field lines, as is the case for the dayside ionosphere, or through the re-

Figure 2.9: Green and red aurora observed south of Longyearbyen, Svalbard, during the night. Image courtesy of Karlotta Kürzel.

connection of open magnetic field lines from each hemisphere in the magnetotail. Upon entering the ionosphere, particles can ionize and excite atmospheric constituents, mainly nitrogen and oxygen. The excited atoms can then relax into their ground state, releasing their energy either kinetically in a collision with another particle, or by photoemission. The photons emitted in this process give rise to the aurora. Figure 2.9 portrays green and red aurora as observed south of Longyearbyen, Svalbard. The image was taken during the night, which is why the sky is dominated by green aurora. However, at higher altitudes red aurora can be seen as well.

Since auroral emissions are due to the relaxation of excited atoms, they have discrete energies (wavelengths). Both green and red aurora stem from electronic transitions in atomic oxygen. Figure 2.10 shows the energy level diagram for atomic oxygen. The

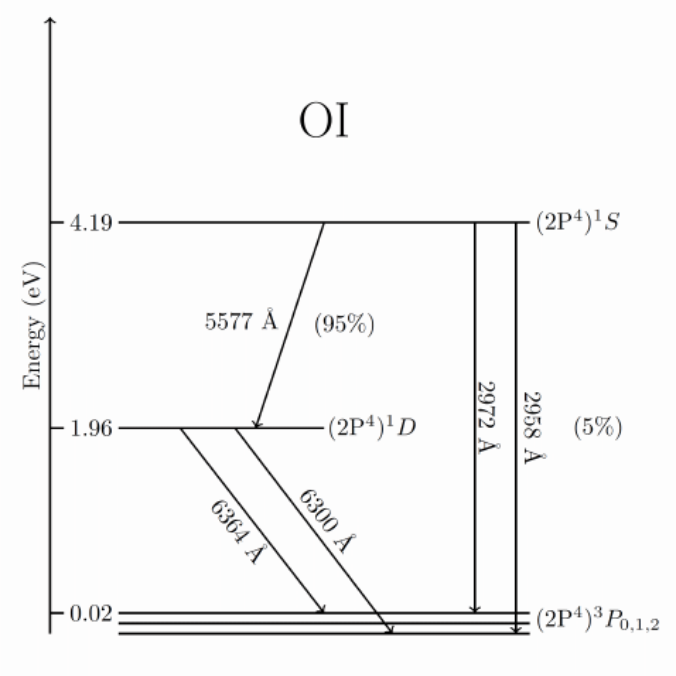

Figure 2.10: Schematic showing the energy level diagram of atomic oxygen [Bhardwaj, 2012].

green auroral emission line is due to the electronic transition from the $(2P^4)^1S$ state to the $(2P^4)^1D$, which is a forbidden transition. This leads to a long lifetime of around one second, as listed in table 2.2. The red auroral emission line is also caused by a forbidden transition in atomic oxygen, namely from the state $(2P^4)^1D$ to the state $(2P^4)^1P$. In this case, the lifetime is even longer at almost two minutes (see table 2.2). These long lifetimes significantly affect the altitude at which green and red auroral emission can occur.

As mentioned above, an excited oxygen atom can relax to the ground state and lose its energy either to a photon, creating aurora, or in a collision. Thus, if the time between collisions is substantially higher than the relaxation time τ, the probability that the excited atom will release its energy in photoemission, giving rise to aurora, is very low. Since the collision frequency decreases with increasing altitude, the peak auroral emission height is higher than the altitude at which most of the energy of precipitating

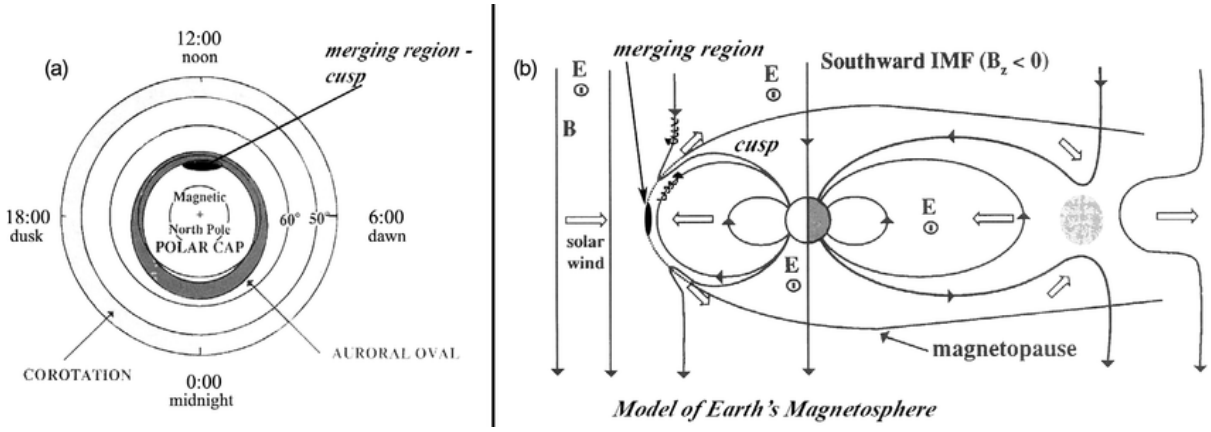

Figure 2.11: Schematic showing (a) plot of auroral oval in magnetic local time coordinate system and (b) magnetosphere showing the precipitation source of the cusp [Hui, 2010].

particles is deposited. This effect is called quenching, and it shifts the peak auroral emission height of the green and red line from about 100 km to 120 km and 240 km, respectively.

Another consequence of the long lifetime of the red emission line is that most oxygen atoms travel many kilometres, some even tens of kilometres before engaging in photoemission. This leads to red aurora appearing more diffuse and blurred, compared to green aurora. Although this difference can be seen in ASC images, it is also very apparent in keograms (see figure 3.1).

Colour	Wavelength λ [nm]	Source particle	Lifetime τ [s]
green	557.7	O	0.7
red	630.0	O	110
blue	427.8	N_2^+	$\sim 10^{-8}$

Table 2.2: Colour of auroral emissions along with their wavelength as well as their source particles and its lifetime in the excited state [Baumjohann and Treumann, 2012, Nozawa, 2018].

2.7.1 Auroral Oval

Aurora occurs in an oval centred around the magnetic pole. This oval is called the auroral oval (see figure 2.11) and it is approximately symmetric along the noon-midnight line, but asymmetric along the terminator. The dayside auroral oval is thinner and closer to the magnetic pole than the nightside oval. It typically extends from 75° to 80° MLAT on the dayside, and from 65° to 75° MLAT on the nightside. However, the exact location of the oval depends on many factors, including the conditions of the IMF, magnetic reconnection, and particle precipitation.

The colour of the aurora is closely linked to the energy of precipitating particles, as the latter determines the altitude range over which the bulk of the energy is distributed. The higher the precipitation energy, the lower down it is deposited, leading to the formation of green and blue aurora. Inversely, soft precipitation (< 1 keV), as for example in the cusp and mantle, leads to the red emission line dominating. On the nightside, the green auroral emission line dominates due to the comparatively high precipitation energy of particles (see section 2.6.2).

Dayside aurora is different in many ways from nightside aurora. As previously mentioned, precipitation energies are typically low, leading to the formation of red aurora at higher intensities than emissions in the green line. The equatorward boundary of the dayside auroral oval is given by the OCB, implying that precipitation occurs almost exclusively on open field lines. Consequently, many dayside auroral phenomena are driven by reconnection of the IMF to the magnetosphere.

2.7.2 Poleward Moving Auroral Forms

This thesis investigates a specific type of auroral occurrence called a poleward moving auroral form (PMAF). PMAFs are auroral arcs that are aligned along magnetic east-

west. They are characterized by poleward motion following their formation inside the auroral oval. The beginning of a PMAF event typically coincides with a brightening of the equatorward boundary (equatorward boundary intensification, EBI) of the auroral oval as well as a slight equatorward expansion of the oval [Sandholt, 1986, Fasel, 1992]. Typical poleward propagation speeds lie at around 500 m/s [Oksavik, 2005]. PMAFs occur exclusively in the dayside polar cap ionosphere around magnetic noon [Lockwood, 1989], which is a consequence of their formation mechanism. It is widely accepted, that PMAFs are the visual signatures of so called flux transfer events (FTEs) [Sandholt, 1986, Fasel, 1992, Xing, 2012, Lockwood, 1989, Wang, 2016]. A FTE occurs during dayside magnetopause reconnection typically following the southward turning of the IMF [Neudegg, 1999, Wang, 2016, Goertz, 1985]. During this process a large quantity of solar wind plasma is heated, accelerated and injected into the magnetosphere. These energetic particles can precipitate into the dayside ionosphere along newly formed open field lines. As these field lines convect towards the nightside, the place at which particles enter the ionosphere moves towards the nightside as well, giving rise to an auroral form that is moving poleward, a PMAF.

Due to the energy enhancement that solar wind particles experience during a FTE, PMAFs are greener than other dayside aurora, yet they can be observed in both the red and green auroral emission lines.

PMAFs have an average lifetime of approximately five minutes [Fasel, 1995], and they frequently occur in sequence. In the case of sequential PMAF events, the average time between two consecutive events is about seven minutes [Fasel, 1995]. A sequence of PMAF events is associated with pulsed reconnection [Hwang, 2020], further supporting the connection between PMAF and FTE events.

As PMAFs are the auroral manifestation of flux transfer events, which rely on dayside magnetopause reconnection, they are expected to occur during southward IMF.

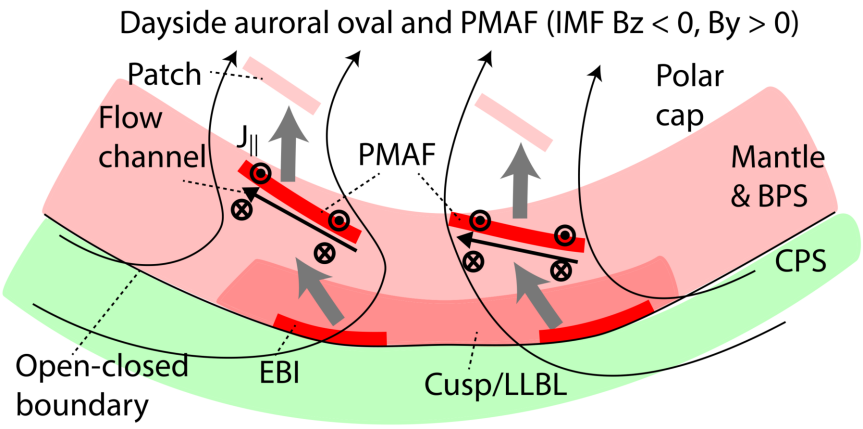

Figure 2.12: Schematic of a pre- and post noon PMAF forming at the OCB causing a EBI and propagating northwards (grey arrows). The small scale current system associated with PMAFs is shown. Figure from Frey et al. (2019).

While PMAF events do seem to occur more often during southward IMF, about 60% of the time, they also do during northward IMF [Xing, 2012, Xing, 2013, Wang, 2016]. Additionally, the IMF By component seems to play a role for the occurrence of PMAFs, as the majority of PMAFs occur during eastward IMF [Xing, 2012, Xing, 2013], suggesting lobe reconnection might be of relevance.

Particle precipitation leading to auroral emissions associated with PMAFs due to electrons at hundreds of eV to 1 keV. While that energy range is still low compared to nightside aurora, PMAFs are generally the highest energy dayside auroral form [Oksavik, 2005, Lorentzen, 2010]. Since precipitation is purely due to electrons, an upward (field aligned) current arises at the location of the PMAF (see figure 2.12). This current is connected to a downward current via a flow channel, leading to the formation of dynamic small scale current system coupling the polar cap ionosphere to the magnetosphere. The connecting horizontal flow channel current is carried by ions. One of the aims of this project is to measure these flow channels during PMAF events.

3 Instrumentation

This thesis uses data taken from a range of instruments including a meridian scanning photometer, all sky cameras, space-based magnetometers and coherent scatter radars. In this chapter, the operating principle of each instrument will be briefly explained.

3.1 Meridian Scanning Photometer

The meridian scanning photometer (MSP) is used to study auroral occurrence and movement along the magnetic meridian. The MSP used for this analysis is located at the Kjell Henriksen Observatory (KHO) on Breinosa, Svalbard. The instrument consists of a mirror that scans the meridian along the magnetic north-south direction in a period of 16 seconds. It possesses four channels, that each consist of a narrow bandpass filter mounted onto a tilting frame in front of a photo-multiplier tube. Three of the four bandpass filters are designed to observe aurora emitted by atomic oxygen (5577 Å, 6300 Å and 8446 Å). The fourth detector measures photon intensities in the molecular nitrogen emission line (4278 Å). The field of view of the MSP is a narrow channel aligned with the magnetic meridian, and is shown along with the fields of view of other instruments used in this project in figure 3.6.

The final measurement consists of the light intensity per 1 degree of elevation per scan for each of the four channels. Commonly, this data is plotted as a so called keogram. A keogram is a two dimensional heat map with time (scan number) plotted on the x-axis, elevation on the y-axis and light intensity colour coded. Figure 3.1 shows an example of a keogram. The different heat maps show light intensities in different channels (wave-

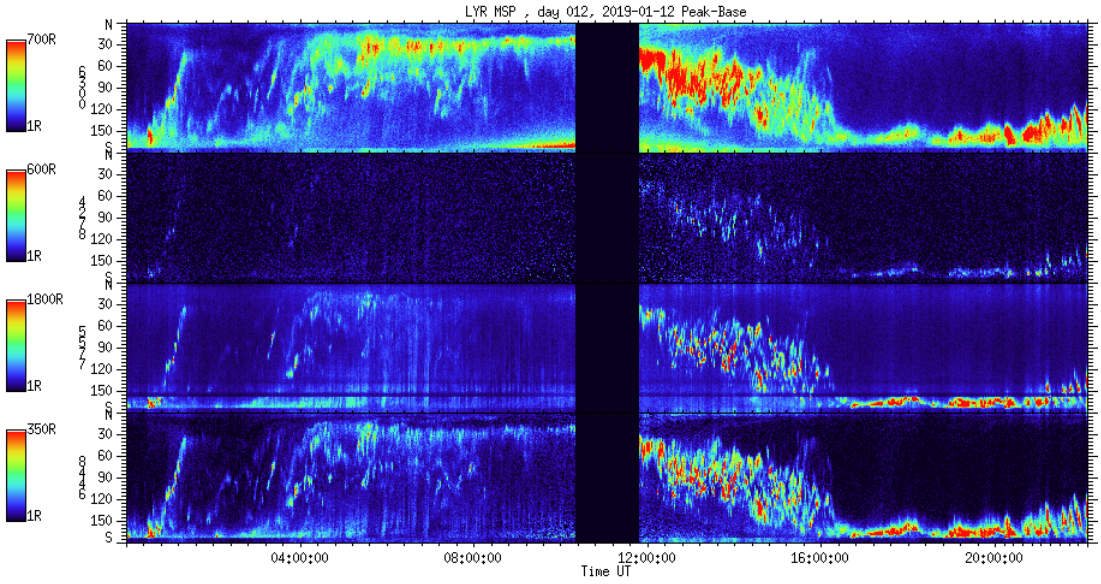

Figure 3.1: Keogram from January 12th 2019. Aurora is easily visible in all channels from 12 to 16 UT. The MSP shuts off just before noon to protect its photomultipliers from being exposed to increased brightness levels as the sun reaches its maximum elevation of -9.9° creating the data gap. The scattered sunlight can be seen close to the southern horizon in the red channel (6300 Å) just before and after the data gap.

lengths). Light intensity (colour scale) is measured in Rayleigh (R), which is defined as:

$$1\,\mathrm{R} = 10^{10}\,\frac{\mathrm{photons}}{\mathrm{m^2 s}}$$

The measured auroral intensity typically ranges from a few hundred Rayleigh to tens of kR, depending on both the actual auroral brightness and the spectral width of the narrow bandpass filter in a given channel. The green (5577 Å) and red (6300 Å) channels are most relevant for this analysis, since those channels have the highest intensities.

The MSP is one of the most important instruments used in this study, as it was used to initially identify PMAFs, as well as determine several of their parameters such as brightness, colour and velocity.

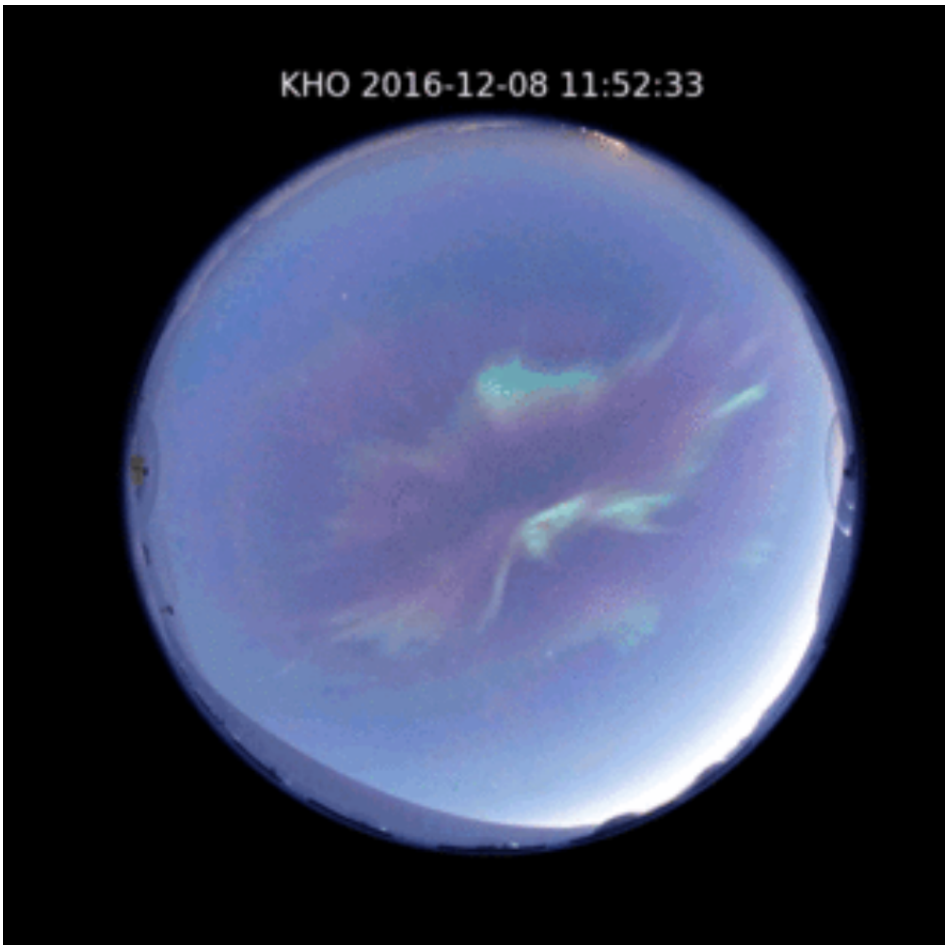

Figure 3.2: Example of an ASC image portraying dayside aurora. Red and green auroral emission can be seen clearly, with emissions dominating in the red line.

3.2 All Sky Camera

All sky cameras (ASC) capture the entire sky in one image in order to allow detailed study of the morphology of auroral forms. The analysis presented in this thesis uses images taken by a Sony α7S full-frame all sky camera with a Sigma 8mm f/3.5 EX DG circular fisheye lens. It takes RGB images and can also be equipped with a narrow band pass filter. The ASC has an exposure time of 4s and a variable time resolution of 12-30s. Ground based ASCs are comparatively cheap and accessible, however they

require favourable weather conditions and have to handle light pollution. One of the ASCs used is set up under a heated dome at KHO while another one is situated in Ny-Ålesund, approximately 120km north-west of KHO. Figure 3.2 gives an example of dayside aurora in an ASC image.

MSPs and ASCs are particularly useful in the effort to manually identify and qualitatively analyse auroral structures. However, manual identification and analysis of auroral forms is very time consuming and subject to human error. For this reason, this project uses an index designed to quantify auroral morphology based on ASC images, known as the arciness index.

3.2.1 Arciness

The arciness index A is a quantitative measure of how much the shape of an auroral structure in an image resembles an arc. The index is a number between 0 and 1 and calculated by an algorithm for a grey scaled ASC image. The algorithm identifies all structures comprised of the brightest pixels in the image and fits each structure with a polynomial. The index is defined as:

$$A = \min\left[\frac{3}{\ln(NM)}, 1\right] \tag{18}$$

where N is the weighed number of dominant auroral structures in an image and M is a measure of the typical deviation of the actual shape of the auroral structure from the fit. M is given by the sum of χ^2-values (goodness of fit parameter) of different auroral structures normalized to the number of pixels in all structures. The fit is a polynomial whose order solely depends upon the number of pixels in the auroral structure that is to be fitted. The order p of the polynomial is given by: $p = \lfloor \log_{10}(n) \rfloor$ where n denotes

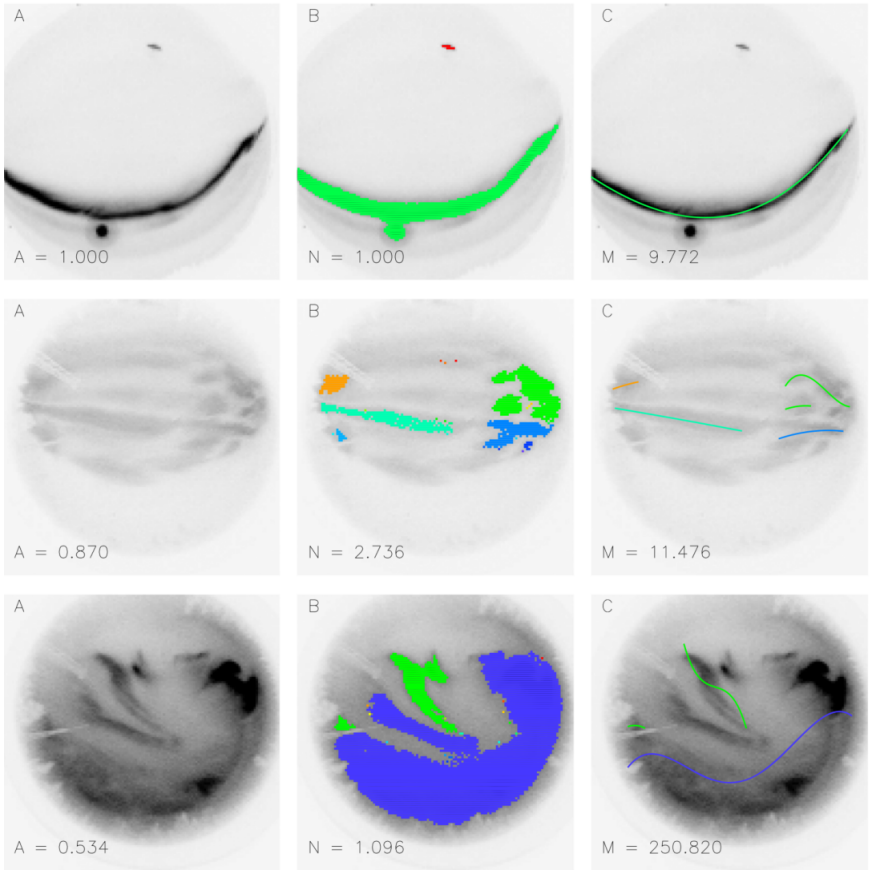

Figure 3.3: Examples of ASC images in an inverted grey scale with the associated arciness value A (a). Weighed number of bright-pixel-clusters N overlaid on original images using colour-coding to distinguish between different clusters (b). Fit polynomials drawn onto original image for each cluster along with the M value of each image (c) [Partamies, 2014].

the number of pixels in the structure [Partamies, 2014].

Due to the the fact that M is a measure of deviation from a fit, wider auroral structures have higher values of M and therefore a higher error and lower arciness index than thinner structures. Additionally, auroral structures whose shape can not neatly be described by a polynomial (e.g. diffuse aurora) have low values of M.

Since N describes the weighted number of structures over which the brightest pixels are distributed, having most bright pixels be concentrated in a single auroral structure (low values of N) leads to high arciness. This can be the case for an auroral arc, as

shown in the top left image in figure 3.3. Inversely, having multiple auroral shapes with similar brightness in the same image causes the arciness to decrease.
It is interesting to note, due to arciness being defined as the minimum (eq. 18), there is an upper bound for arciness. This upper bound is $A = 1$, and it is reached very often, up to more than half of the time in the dusk sector [Partamies, 2014].
Arciness has been used to investigate auroral forms occurring between 16 - 10 UT, however it has never been used to study the dayside and PMAFs.

3.3 Solar Wind and IMF Measurements

NASA's Goddard Space Flight Center provides an open access database called OMNI-Web, which includes near Earth IMF and solar wind data. A range of different satellites in orbit around L1 are responsible for data collection, including ACE and Wind. They are equipped with multiple instruments designed to study the solar wind and IMF, such as magnetometers, spectrometers and Faraday cups, among others. The satellites provide low resolution (1 hour) and high resolution (1 min) data on solar wind and IMF parameters. The data are time shifted to the magnetopause. In this thesis, we will focus on GSM IMF components as well as solar wind speed, temperature and density.

3.4 SuperDARN

The Super Dual Auroral Radar Network (SuperDARN) is a system of 35 high frequency coherent scatter radars situated in the northern and southern hemisphere (see figure 3.4). SuperDARN is used to study a variety of phenomena, including the global polar ionospheric convection pattern, smaller scale flows, such as flow channels and reverse flow events, and field-aligned currents (FACs) among many others. For this project,

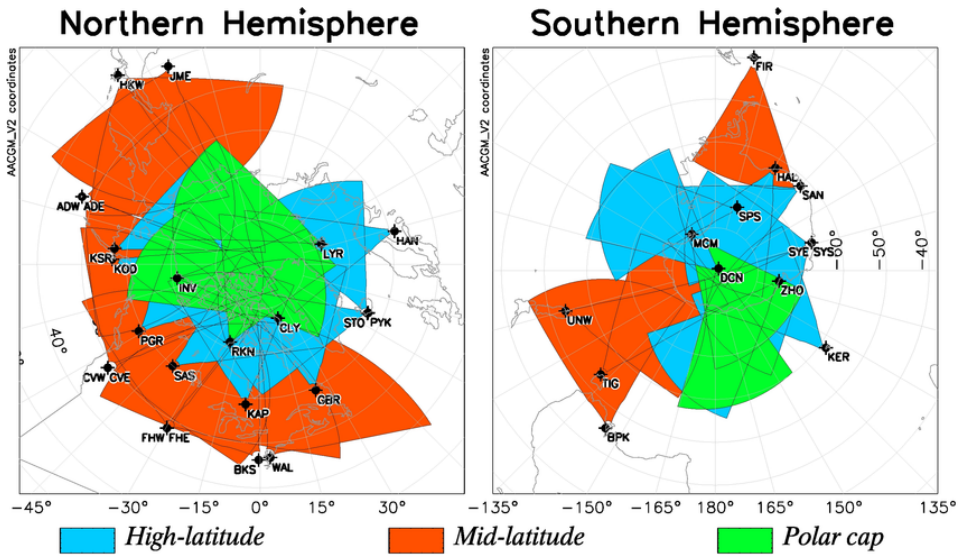

Figure 3.4: The fields of view of all SuperDARN radars in the northern (left) and southern (right) hemisphere colour-coded according to their latitude. Figure from Nishitani et al. (2019)

the Hankasalmi SuperDARN radar in Finland will be used to investigate the occurrence of flow channel events (FCEs) in relation to PMAF activity detected by optical instruments that were introduced earlier in this chapter.

The Hankasalmi radar, as well as all SuperDARN radars, consists of two arrays of electronically phased antennas: the primary (main) array, including sixteen antennas, and the secondary array serving as an interferometer. A short pulse sequence is transmitted from the radar into its field of view. This signal then propagates through different layers of the atmosphere and can be scattered at plasma density enhancements in the E- or F-region of the ionosphere back towards the radar. Most of the signal, however, is not reflected towards the radar and can propagate further to be reflected at another location in the ionosphere or by the ground. This enables the radar to detect backscatter from many different distances; in the case of SuperDARN, typically from 180 km to more than 3500 km from the radar.

Figure 3.5: Aurora seen over the Saskatoon SuperDARN radar site. (Credit: Ashton Reimer)

These plasma density enhancements (also referred to as irregularities) that the radar signal scatters at can be the result of different phenomena. In the F-region, these irregularities can form as a consequence of electron density enhancements caused by solar UV or particle precipitation associated with aurora. Ultimately, these irregularities can be detected by SuperDARN radars through Bragg scattering, leading to constructive interference of scattered waves (the addition of coherent waves; coherent scatter radar). The received signal is then compared to itself with varying lags using a technique known as autocorrelation. This technique results in a complex autocorrelation function (ACF), from which three main parameters are derived. The spectral width and power are determined from the magnitude of the ACF, while the line-of-sight velocity is inferred from the phase of the ACF. For this study, localized short term enhancements in the line-of-sight velocity are used to detect flow channels in association with PMAFs.

The Hankasalmi radar possesses sixteen beams each covering an azimuthal range of 3.3°. This gives the radar a total azimuthal field of view of approximately 53°. The

spatial resolution of SuperDARN allows the radar to take measurements in 45 km increments in the line of sight direction, so called range gates. In the azimuthal direction, the spatial resolution is variable, decreasing linearly with distance.

The degree to which accurate measurements of small scale flow channels and similar can be made is severely limited by this spatial resolution. PMAFs, as well as many types of associated flows, exist on scales of tens to no more than a hundred km latitudinally. This implies, that these phenomena can only affect one or two range gates per beam (when the line-of-sight direction is (roughly) aligned with magnetic north, as is the case in this study).

Not only does the spatial resolution of SuperDARN limit the extent of this study, but so does the time resolution. SuperDARN has a time resolution of one to two minutes, while the average lifespan of the PMAFs in this study is approximately five minutes. This presents similar obstacles that need to be overcome in order to use SuperDARN to measure small scale dynamic structures.

Furthermore, there are other inherent limitations and errors that SuperDARN introduces that need to be considered before analysing the data. Sources of these limitations and errors are hardware, software, and external sources associated with HF radiation and near-Earth space. Most importantly, in order for measurements of a certain region of the ionosphere to be made, there need to be irregularities to scatter from. This means for this study, that electron densities caused by auroral precipitation need to be intense enough to create sufficient backscatter.

Moreover, SuperDARN employs a method to determine the location of the backscattering region, that is based on the straight line distance and a set virtual height. Temporal and spatial fluctuations in the ionosphere can introduce mapping errors. It has been estimated, that this can lead to an inaccuracy of 20-60 km in the determination of the backscatter location [Yoeman, 2001].

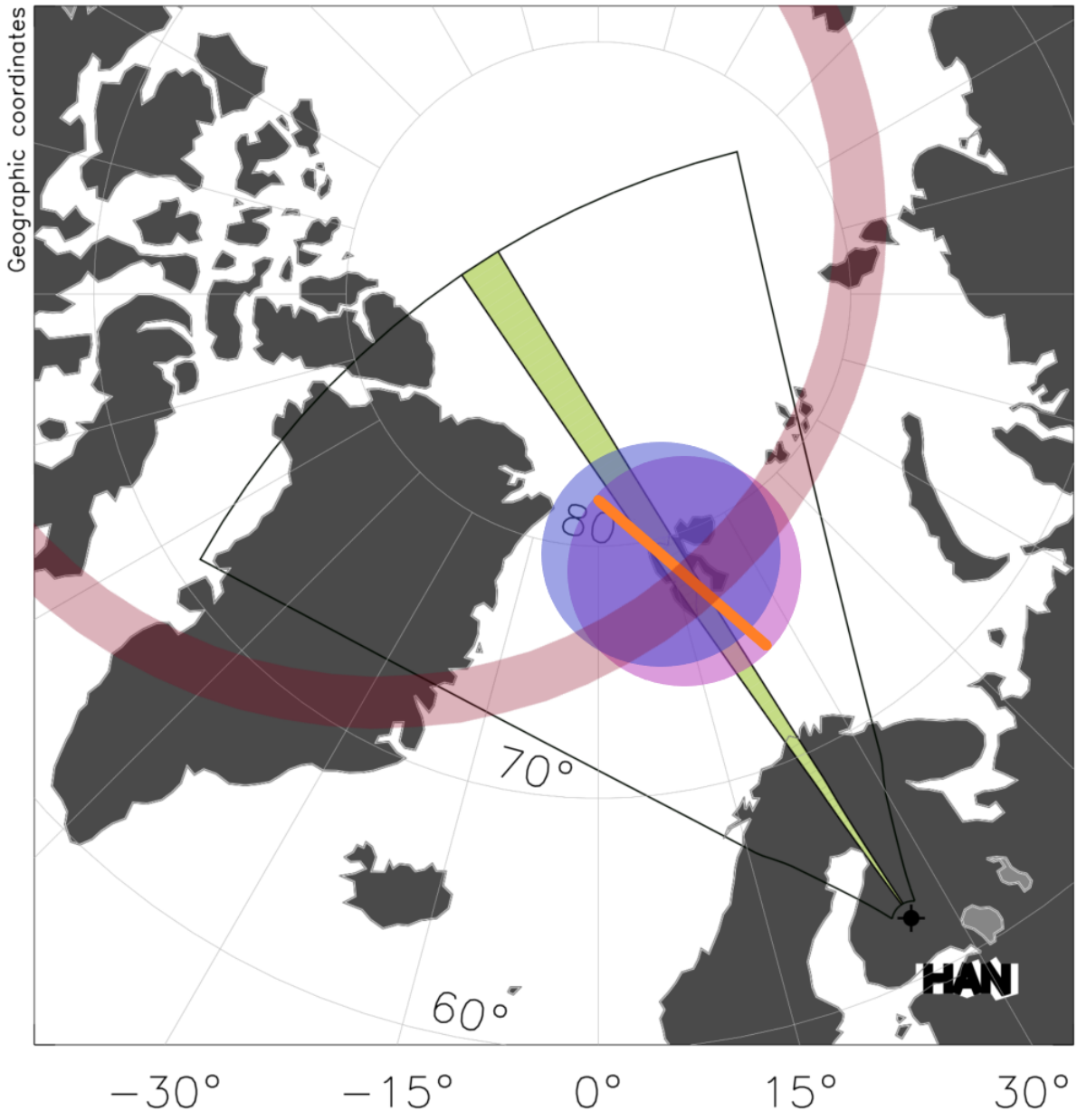

Figure 3.6: Map of the north polar regions showing fields of view of the Hankasalmi radar (delimited by the black line) with its ninth beam (green), the Longyearbyen and Ny-Ålesund ASCs (purple and blue, respectively) and the Longyearbyen MSP (orange). The average position of the auroral oval (dark red) is shown for 12 MLT in Svalbard.

These are the the most important limitations associated with SuperDARN for this project. Understanding these limitations aids to properly interpret the data.

4 Methodology

Before the results of this thesis will be presented and discussed, the forming of event lists and data processing techniques will be explained in this chapter. This includes the initial identification of PMAFs based on keograms and the forming of event lists according to data coverage of different instruments. Afterwards, all analysis techniques and algorithms used will be described, some of which are widely used, such as the superposed epoch analysis. Others were developed as part of this project, such as the algorithm that determines the velocity of PMAFs.

4.1 Identification of PMAFs

The initial identification of PMAFs was accomplished by manual inspection of keograms. PMAFs manifest themselves as distinct structures in the red (630.0 nm) and green (557.7 nm) channels of a keogram. Their poleward motion causes them to appear in a keogram as a diagonally aligned band that fades over time. All keograms in this thesis show time along the x-axis and scan angle / elevation (or latitude) on the y-axis, where elevations above 90° correspond to northern directions. Thus, PMAFs manifest themselves as bands stretching towards the upper right of their starting position in the auroral oval, as can be seen in Figure 4.1, which shows a PMAF in the red and green channels of a keogram. The PMAF occurs at approximately 06:50 UT lasting 5 minutes. Its track is shown in both channels as a black line and was determined using an algorithm, which will be discussed in section 4.3. The y-axis has been reformatted to show altitude-adjusted geomagnetic latitude (AAMLAT) on a linear scale, as opposed

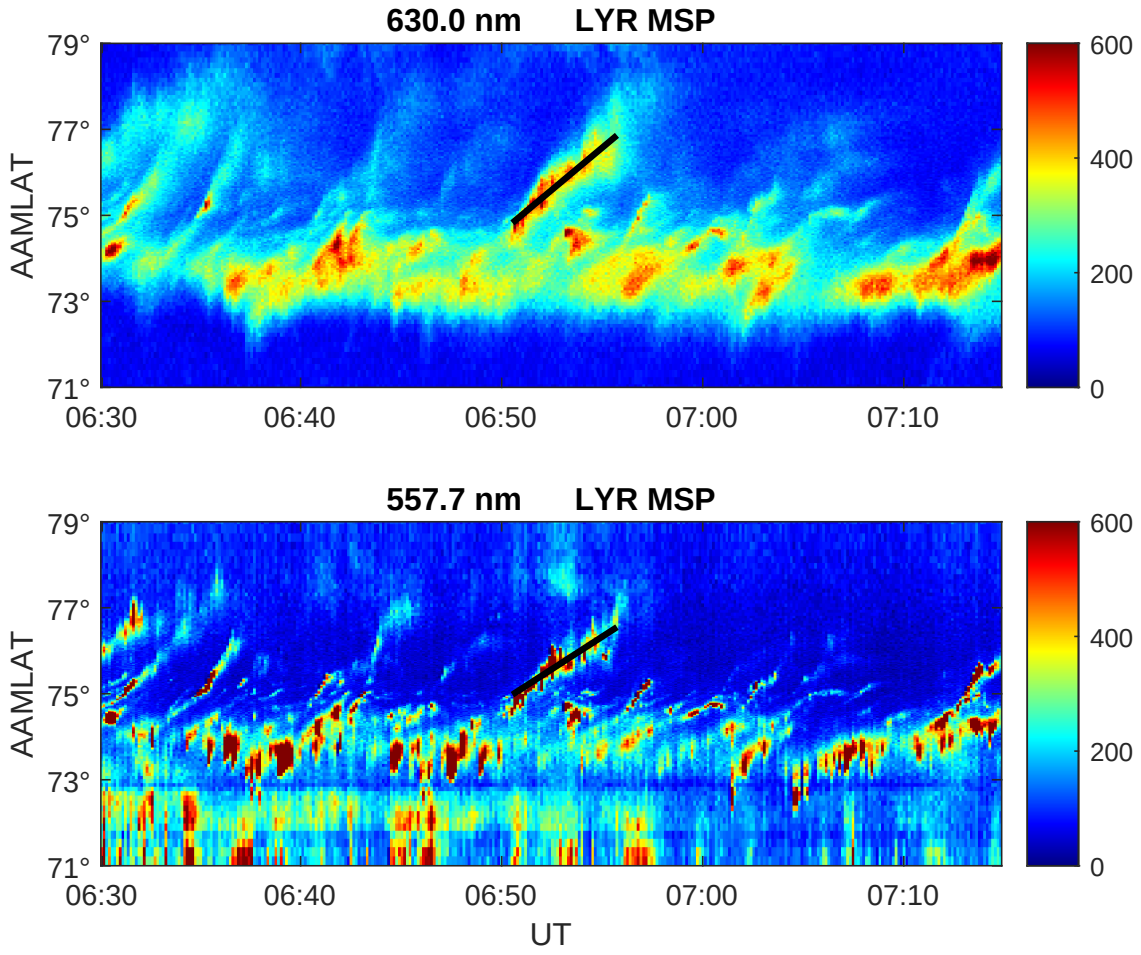

Figure 4.1: Keogram of PMAF event observed using the MSP at KHO on the 18th of December 2017.

to showing scan angle linearly. The green and red channels both show strong auroral emission associated with the PMAF, detaching from the auroral oval, which is situated at approximately 73° to 75° AAMLAT. The PMAF moves poleward by about 2° before fading at around 06:55 UT.

During the identification of PMAFs, several criteria would have to be met in order for a candidate event to be considered a PMAF event:

- Auroral emission in the red and green channel at intensities significantly greater than typical noise levels.

- Poleward motion starting from inside or close to the auroral oval.
- Clear spatial separation between the PMAF candidate and other auroral emissions near the end of the candidate's lifetime.
- Occurrence within a time window of three hours before to three hours after magnetic noon (9-15 MLT, 6-12 UT).
- Event lifetime from 1 to 20 minutes.

As PMAFs occur around the noon sector, they can only be observed by the optical instruments during the polar night. This narrows down the measurement time frame to approximately two months per year, from the end of November to the end of January. During other times of the year, there is too much (scattered) sunlight in the sky for dayside auroral emissions to be detected by the MSP. Cloudy days and times during which the MSP is shut down further narrow the measurement time frame. This leads to smaller numbers of individual PMAF events that can be analysed, despite PMAFs being a common auroral feature.

For each PMAF event, start and end times were recorded and listed. The event lists are based on data coverage of different instruments. This thesis statistically analyses three different event lists, the first event list consisting of 23 PMAFs that occurred between 2003 and 2008. In addition to the requirements every PMAF candidate has to meet, the events in this event list had to have been observed by two ASCs, one at KHO and one in Ny-Ålesund, and the MSP at KHO. The algorithm calculating arciness (see section 3.2.1) has been applied to ASC images from both cameras used in this thesis from 1999 to 2009, which constrains the time frame of this event list. This event list was analysed in terms of arciness, which was the first time the arciness index was used to quantify dayside auroral structures. For this dataset, the arciness algorithm uses

grey-scaled images taken by ASCs that had a narrow band pass filter for the green auroral emission line mounted onto them. The arciness that was calculated in this manner will be referred to as (green) channel arciness.

This is different from the way the arciness in the second event list is determined. In the second event list, the arciness algorithm is fed the green (red) component of RGB images that were taken without a narrow band pass filter, which will be referred to as colour arciness. This event list consists of 18 PMAF events that all occurred on the 18th of December 2017. It is extremely unusual for that many events to occur on a single day. Typically, only a small handful (0-5) of PMAF events can be observed in a single Earth-bound location on a given day. As part of the initial identification of PMAFs using MSP data from KHO, over two decades of keograms were manually inspected, and there was no other date that showed close to that many PMAF events. For this date, MSP, ASC and arciness data from KHO, as well as solar wind and IMF data were analysed. Due to the fact, that this day is extremely special in terms of PMAF occurrence, the first and second event lists are not combined, even though they have the same data coverage. Combining the first and second event lists would introduce bias into the sample, where nearly half of all events occurred on a single day, meaning the particularities of that day would be heavily over-represented. Hence, event lists 1 and 2 are analysed separately, however their results are nevertheless compared and differences between them discussed.

Finally, the third event list includes 9 PMAF events that occurred on the 10th of December 2013. The events were recorded by the KHO MSP and the SuperDARN radar in Hankasalmi, Finland. This enables study of the PMAF velocity in relationship to the ionospheric plasma convection speed, which can give insight into how currents flow around PMAFs. The details of each event list, such as number of PMAFs, instruments used etc., are summarized in table 4.1.

Event List	1	2	3
Number of PMAFs	23	18	9
Number of Days	10	1	1
Optical Instruments used	MSP, ASC	MSP, ASC	MSP
Radars used	none	none	SuperDARN Hankasalmi
Solar Wind & IMF data analysed	yes	yes	yes

Table 4.1: Table showing different properties of each event list analysed, such as number of PMAFs and days, as well as different data sources.

4.2 Superposed Epoch Analysis

The most commonly used data analysis method of this thesis is the so called superposed epoch analysis (SPEA). A SPEA is used to extract what is common across all members of a class (for example PMAF events). This is accomplished by dividing all events up into the same number of time intervals, and averaging some parameter describing the events within the same intervals. A common example of this method is dividing individual days in a year into 24 one hour intervals and averaging the temperature measured in each hour across all days. The resulting curve describes the evolution of temperature over the typical day. Any statistical fluctuations that are present in individual days will cancel out as the number of days increases. Similarly, seasonal variations in temperature will not show up in the result of the SPEA, only commonalities in all events do. In our example, this might be an increase in temperature in the morning, a maximum just after noon, and a decrease in the evening.

For this thesis, SPEAs were employed to investigate the evolution of different parameters during the occurrence of a PMAF. These parameters are arciness, auroral brightness

in the green and red channels, their ratio as a proxy for precipitation energy, and several quantities describing the conditions of the IMF and solar wind. As not all PMAF events are equal in duration (lifetime), they are normalized in order to enable comparison using SPEAs. In this analysis, not only the timespan in which a PMAF occurred is considered, but also one PMAF lifetime before the beginning and one lifetime after the end of an event.

In a SPEA, as the number of intervals in one event lifespan is divided up into increases, the time resolution increases, but statistical fluctuations of the curve increase as well, as fewer data points are averaged in each interval. Hence, deciding the number of intervals events are divided into is a trade-off between time resolution and the minimization of statistical errors. For this thesis, there are usually three or four time intervals per PMAF lifetime, which corresponds to a time resolution of approximately 1-2 minutes. As different instruments have different time resolutions (MSP has 8-16 second resolution, while IMF data is 1 minute resolution), the number of intervals chosen also depends on the instrument with which the parameter that is analysed was measured by.

4.3 Determining PMAF Position and Velocity

The event lists that were manually created for this analysis include start and end times delimiting the lifetime of the auroral emissions associated with the PMAF events. However, they do not include information about the position of the PMAFs and their motion over their lifetimes. The latitudinal position of PMAFs was determined by an algorithm developed for this thesis.

This algorithm considers each scan of the MSP taken within the PMAF lifetime individually. Within each scan, it finds the position of peak intensity in the red channel,

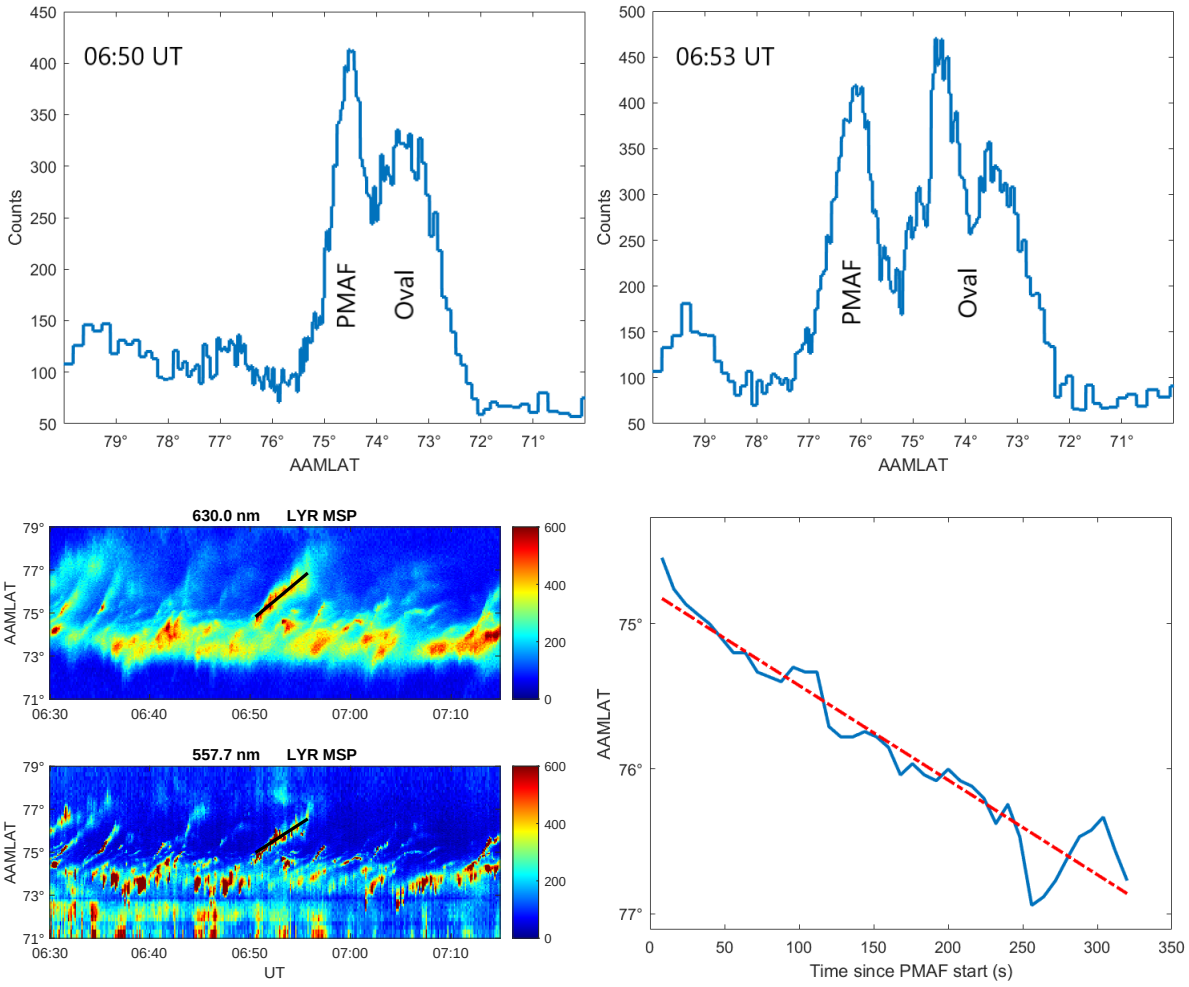

Figure 4.2: Several plots showing how the algorithm calculates the position of a PMAF. In the lower left corner the red and green channels of a keogram are shown with a PMAF event occurring between 06:50 and 06:55 UT, as indicated by the black line. The top row shows the auroral intensity in the red channel of individual scans at the beginning of the PMAF event (left) and near the end (right). In the left plot, the peak in intensity corresponding to the PMAF is still close to the auroral oval, as the PMAF is emerging from the oval. Later on (right side), the PMAF has advanced to more than 76° AAMLAT. The lower right plot shows the position of peak intensity (blue) and its linear fit (red). This fit is also plotted in the keogram (black line) in both channels.

as shown in figure 4.2. Generally, from one scan to the next, this position of maximum brightness moves polewards due to the motion of the PMAF, however this is subject to

fluctuations. Frequently, the auroral emissions associated with PMAFs are weaker than emissions from the auroral oval (see fig. 4.2, top right). For this reason, the algorithm ignores all aurora further than 50 km equatorward of the position of peak intensity of the previous scan, ensuring that the algorithm measures the position of the PMAF rather than the auroral oval. This distance of 50 km was chosen as it corresponds to the typical latitudinal width of a PMAF.

Once the algorithm has determined the position of peak intensity for all scans within the PMAF lifetime, it fits that position as a function of scan number (time) with a linear regression equation (see lower right of fig. 4.2). The resulting linear equation approximates the motion of the PMAF, while the slope of that function corresponds to the velocity of the PMAF.

The algorithm can be thrown off guard by scattered moonlight, clouds or other auroral emissions, which can all produce high intensities in the red channel. In this case, the algorithm can be provided a minimum and/or maximum latitude to consider, excluding other sources that might interfere with its measurement of a PMAF.

The green channel is not used to determine PMAF position, as emissions in the red channel are more diffuse, enabling what has been found to be a more reliable and stable measurement of PMAF position and velocity.

5 Results and Discussion

Most phenomena in space physics are part of complex systems that are influenced by a large number of different mechanisms. The driving conditions behind these systems frequently interact with one another and can be challenging to accurately measure. Moreover, the measurement process is complicated further by the broad range of instruments of different nature used in this field, that introduce errors into the data based on their inadequacies and inherent assumptions. This implies, that the analysis of the data has to be completed with a high level of scrutiny.

In this chapter, the results of this thesis will be presented and discussed. This thesis deals with the dynamics and occurrence of PMAFs: the optical phenomenon (structure and evolution, brightness, colour, position, velocity etc.), the driving conditions (IMF, solar wind, particle precipitation) and their role in magnetosphere - ionosphere coupling, the measurement of ionospheric flow channels.

The first study that will be presented covers the arciness index and its relation to dayside aurora and PMAF occurrence. This is the first time arciness is used to investigate dayside auroral morphology, as so far, arciness has only been used to study nightside aurora [Partamies, 2014]. The goal of this study is to understand the behaviour of the arciness index in relation to PMAF events, to ultimately enable the development of an automated PMAF detection mechanism, based on the arciness index.

Secondly, the brightness in the red and green channels of the MSP is studied. As PMAFs are believed to be triggered by FTEs, typical energies of precipitating particles are expected to be high compared to other dayside precipitation, leading to mostly

green auroral emissions [Lorentzen, 2010]. The green-to-red brightness ratio of PMAF aurora is measured to test our understanding of their formation.

The IMF and solar wind conditions during PMAF events are analysed using SPEAs. It is generally accepted, that PMAFs occur preferentially during negative IMF Bz (southward IMF). Moreover, it is not only the value of IMF Bz that is relevant for PMAF formation, but it is the decrease in Bz or sometimes the southward turning of the IMF, that is critical for a PMAF to form [Xing, 2012, Xing, 2013, Wang, 2016, Fasel, 1995, Drury, 2003]. The value of the IMF By component also seems to play a role, where higher values of By seem to make PMAFs more likely to occur. Additionally, By has been found to strongly influence the local time, at which PMAFs occur [Xing, 2012]. It is not only the IMF, which determines PMAF formation, solar wind conditions might have an impact too. There has been speculation about PMAFs potentially being triggered by short term dynamic pressure enhancements in the solar wind [Sibeck, 1990, Sibeck, 1992]. Hence, the behaviour of the IMF GSM coordinates and solar wind parameters are investigated.

Oksavik et al. (2005) estimated the velocity of a PMAF to be around 500 m/s, which was in line with the ionospheric convection speed in the same region measured by SuperDARN. This is the only study to reporting the measurement of the poleward propagation speed of a PMAF to date. As part of this thesis, an algorithm determining the velocity of PMAFs has been applied to 24 events, significantly expanding the database. Six of these events were also observed by the Hankasalmi SuperDARN radar measuring convection speeds in the polar cap. During those events, enhanced poleward flow can be observed. These are frequently referred to as flow or convection channels, pulsed ionospheric flows or poleward moving auroral radar forms (PMRAFs), depending on their exact characteristics [Frey, 2019]. In this thesis, six sequential PMAFs associated with flow channels are studied.

5.1 Arciness Index

The first part of this thesis concerns the relationship between the arciness index and PMAF occurrence. PMAFs are auroral arcs and occur exclusively on the dayside, while arcs are generally more commonly observed on the nightside [Partamies, 2014]. Thus, it seems reasonable to expect the arciness index could be used to identify PMAFs. The motivation behind this analysis is to enable the development of an automated algorithm, that is capable of identifying PMAFs based on arciness data. The first approach of this study was to consider and compare arciness values of PMAF events and the remaining dayside aurora.

5.1.1 PMAF and Dayside Arciness

The arciness index A is a quantitative description of how arc-like an auroral structure is. As explained in detail in section 3.2.1, arciness is mainly dependent on two aspects:

1. The more structures the brightest pixels of an image are distributed across, the lower the arciness.

2. The better a given structure of bright pixels can be described using a polynomial, the higher the arciness.

PMAFs are expected to coincide with higher values of arciness, as they are bright arcs, that should be well approximated by a polynomial. Additionally, auroral emissions associated with PMAFs are primarily green, while other dayside aurora is mainly red [Lorentzen, 2010]. Since arciness (in the first event list) is calculated from images taken with a green narrow band filter, this will lead to higher values of arciness too, as the brightest pixels are overwhelmingly concentrated in the PMAF. If a red filter had been used,

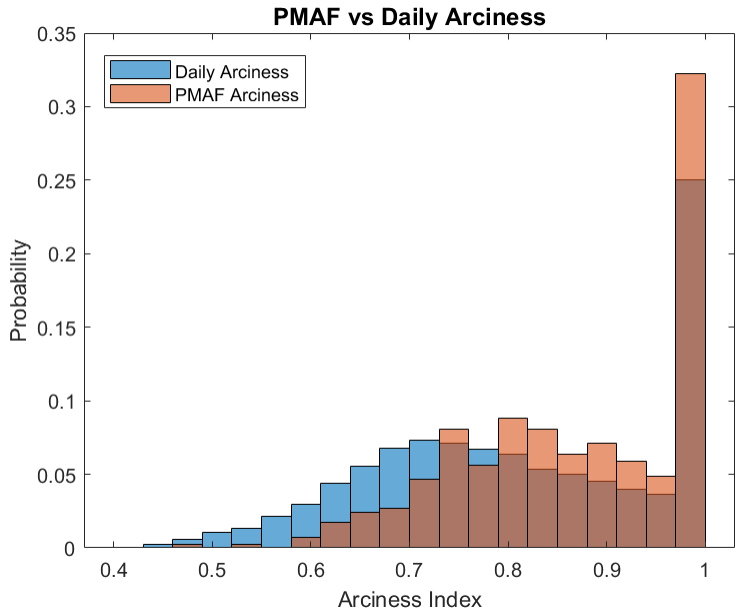

Figure 5.1: Arciness values during PMAF events (red) and daytime baseline (blue)

other types of aurora that show up in the images would be home to many of the brightest pixels, leading to lower arciness.

Figure 5.1 shows normalized histograms of arciness of PMAFs in the first event list (red) and of their baseline (blue). This baseline is comprised of all arciness values between 6 and 12 UT on all days in the event list, except the times during which a PMAF occurs. As seen in figure 5.1, PMAF arciness tends to be higher than general dayside arciness, however, this difference is quite small. The mean PMAF arciness is approximately $\bar{A}_{\mathrm{PMAF}} = 0.86$ while the mean baseline value is $\bar{A}_{\mathrm{baseline}} = 0.81$, a difference of roughly 0.4σ (The standard deviation of both distributions is $\sigma = 0.14$). This means, there is great overlap between typical arciness values during PMAF events and the baseline. Therefore, it is not possible to identify a PMAF merely based on the value of the arciness index itself.

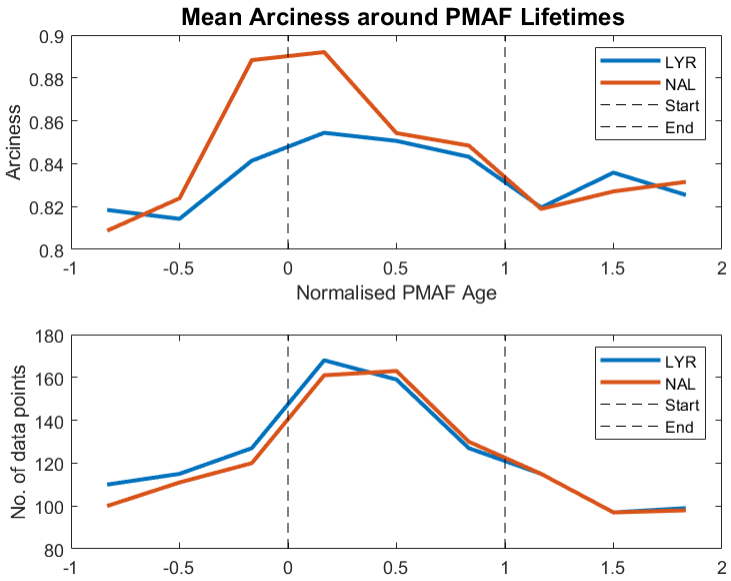

Figure 5.2: Superposed epoch analysis of channel arciness for several PMAF events. Arciness calculated from ASC images taken in Ny-Ålesund (red) and Longyearbyen/LYR (blue).

5.1.2 Superposed Epoch Analysis During PMAF events

A somewhat more complex approach considers the evolution the arciness index goes through over the course of a PMAF event. This approach is based on the assumption that even though the arciness index might not have particularly different values during PMAF events from the baseline, there might be a common evolution arciness goes through in each event. In order to determine wether this is the case, a SPEA was employed to analyse the behaviour of arciness during the 23 PMAFs in the first event list. The result is shown in figure 5.2.

The upper plot shows the evolution of the arciness as a function of the PMAF age, starting from one PMAF lifetime before the beginning of the event to one lifetime after its end. The event time frame is delimited by dashed lines on both sides. Arciness has been calculated and analysed for ASC images taken from both KHO/Longyearbyen

(blue) and Ny-Ålesund (orange). The lower plot shows the number of data points that contribute to each bin and is considered for quality assurance purposes. During the forming of the event list, it was a requirement that every event had arciness data for at least half the event time. However, no such requirement existed for the periods just before and after the event, which is why the number of data points peaks in the event time frame.

The arciness curves for the KHO and Ny-Ålesund data show a similar evolution: an increase in the arciness half a PMAF lifetime before the start of the event, a peak just after the start time, and a subsequent decay towards the baseline value near the end of the PMAF life. Yet, there is one slight difference in the two curves. Ny-Ålesund arciness seems to increase to a larger degree during the beginning of the PMAF. Since the baseline (outside the event time frame) arciness is identical for both stations, the increase is related to PMAF occurrence. Since Ny-Ålesund is approximately 120 km north of the KHO, the ASC has a slightly different field of view (see fig 3.6). This implies that the auroral oval, which a given PMAF separates from near the start time of the event, will be closer to the horizon. Hence, fewer of the brightest pixels will be part of the auroral oval and more will be focussed in the PMAF itself, leading to higher arciness. The baseline, however, is unaffected by this, as the arciness of the auroral oval (without PMAFs) will be the same, independent of its location in the sky.

In order to understand the behaviour of the arciness index in relation to PMAF events (fig. 5.2), it is highly instructive to consider the typical evolution of PMAFs in ASC images. Figure 5.3 shows six ASC images taken with a narrow band pass filter ($\lambda = 557.7\,\mathrm{nm}$) of the same PMAF in different stages of its development. Image (a) shows the bright auroral fragments aligned along an east-west stretching band just before the birth of the PMAF. The different fragments merge into a singular arc in image (b), which begins to move poleward (c). The merging of multiple fragments into a singular

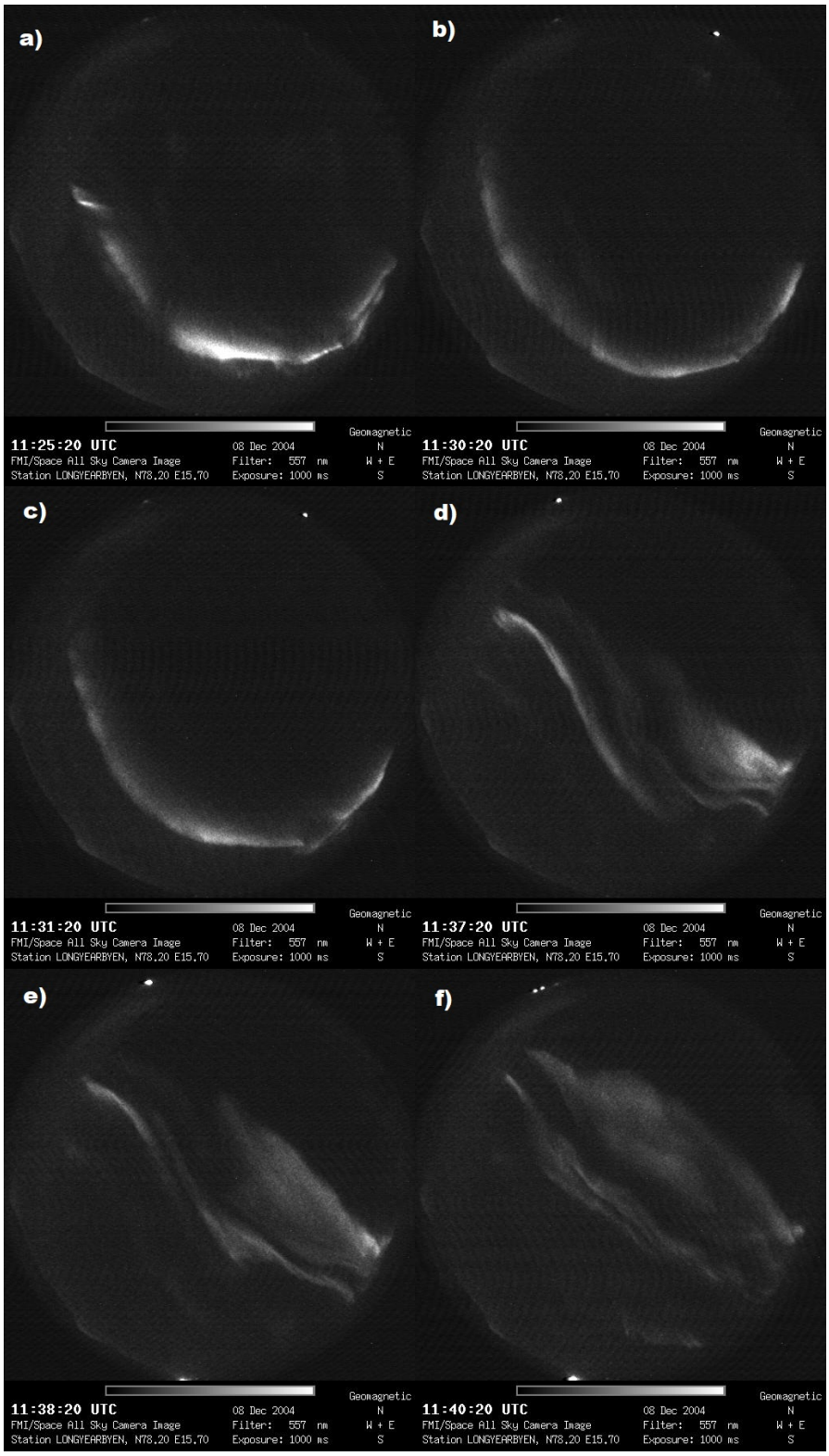

Figure 5.3: Several ASC images portraying the typical evolution of a PMAF.

arc significantly reduces the number of structures bright pixels are distributed across. Additionally, although not clearly visible in fig. 5.3, the equatorward boundary intensification (EBI) increases the brightness in the auroral oval, causing a higher percentage of brightest pixels to be in the auroral oval. Those two effects combined, the combining of multiple fragments into an arc, and the brightening associated with the EBI, lead to a sudden increase in arciness around the beginning of the PMAF lifetime.
As the PMAF fully separates from the oval, the arciness starts to decrease again, as the separation increases the number of structures in the image. During the poleward motion of the PMAF, the latitudinal width of the arc increases and it can split into multiple arcs of varying brightness (d). Both of these factors lead to arciness decreasing further. Near the end of the event, the PMAF begins to lose its arc-like shape and spreads out to gradually becomes more diffuse, causing a final drop in arciness around the end time (e). Finally, auroral emissions (in all wavelengths) fade as the PMAF dies (f) and the arciness returns to its baseline.

In order to put this newly found relation between arciness and PMAF occurrence to the test, the same analysis was conducted with the second event list, which includes 18 events that occurred on a single day. On this day, however, the ASC at KHO wasn't equipped with a narrow band filter. Instead, the arciness algorithm is fed the green (red) component of the rgb colour images. As previously mentioned, the arciness values calculated in this manner will be referred to as colour arciness, while the original kind (narrow band filter) will be called channel arciness. The key differences between the ASC images taken with and without narrow band filters, are firstly, concerning the signal, that the green component of the colour image contains aurora of both the green and the red emission line, while images taken with a green narrow band filter only include green aurora. Secondly, concerning the noise, filtered ASC images only contain a small amount of noise coming from that narrow range specified by the filter, while

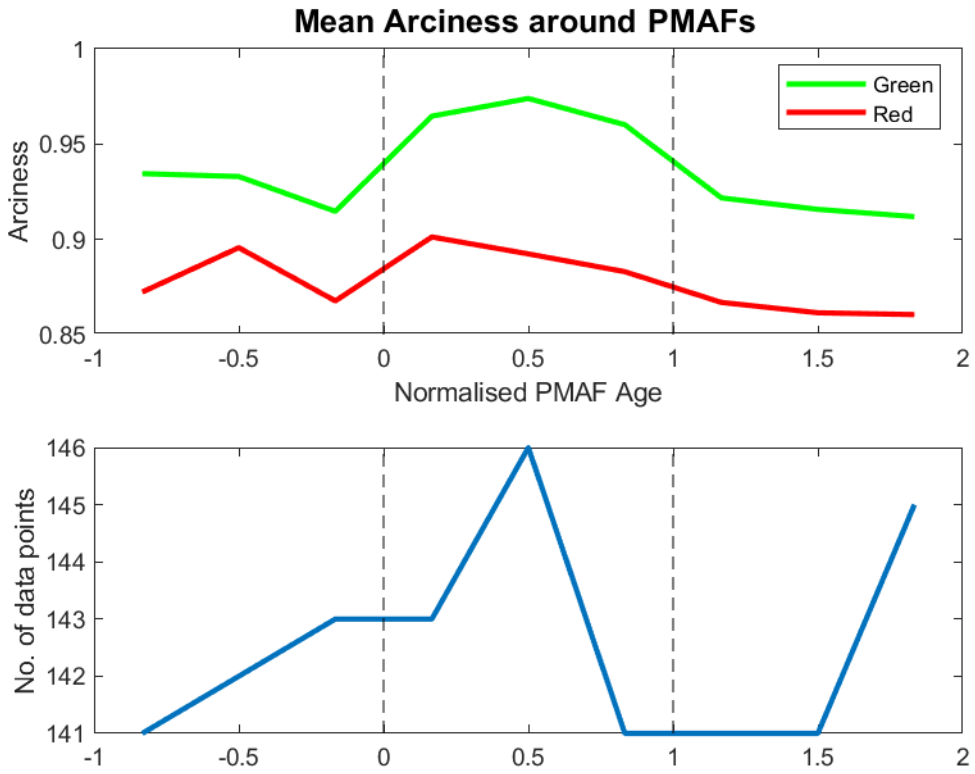

Figure 5.4: Superposed epoch analysis of colour arciness for event list two PMAFs.

any given colour-component of no-filter images will include noise from all wavelengths and from any source. This implies, that, unsurprisingly, filtered images have significantly better signal to noise ratios compared to their unfiltered counterparts.

Figure 5.4 shows the result of a SPEA applied to green and red colour arciness for event list two PMAFs. The general evolution of green colour arciness and channel arciness seems to be almost identical: increasing arciness towards the beginning of the event, a peak during the event, and a decay towards the end. In principle, the red colour arciness follows the same curve. The increase in arciness is much weaker though, which has to do with the relative emission strength of the auroral oval and the PMAF. In the green emission line, the PMAF is much brighter than the auroral oval, whereas they

are similarly bright in the red channel. Additionally, due to the higher lifetime, red emissions associated with the PMAF are more diffuse, leading to a broader distribution of bright pixels in the ASC image. Consequently, red colour arciness does not rise by the same amount.

In summary, the arciness of PMAFs is not particularly different from the rest of the dayside aurora. However, there does seem to be a common evolution arciness goes through during PMAF events. This evolution can be well understood by analysing ASC images the arciness was calculated from. This relation between arciness and PMAF occurrence seems to be robust in regards to variations in the manner in which arciness is calculated, such as utilizing different all sky camera setups, or considering different components of colour images to feed to the arciness algorithm. Thus, these results suggest, this relation could be used to identify PMAFs.

Furthermore, the arciness index appears to be a good indicator of dayside auroral structure, as both arciness values and changes in it can be linked to the morphology of auroral forms. Partamies et al. (2014) showed that the occurrence of auroral arcs is strongly correlated with arciness in the night, dawn and dusk sectors of the ionosphere. This study confirms, that this holds true for the dayside as well. Moreover, (green) colour and channel arciness seem to behave in an almost identical manner, suggesting they may be used concordantly.

5.2 Brightness and Colour of Auroral Emission

While dayside aurora is dominated by the red emission line, green aurora is also frequently observed. Generally, red aurora occurs at roughly twice the altitude green aurora is observed at. The colour of any given auroral form is determined by the energy of precipitating particles that give rise to that auroral form. The higher the precipitation energy, the lower the altitude at which that energy is deposited leading to the formation of more intense green aurorae. Inversely, the lower the precipitation energy, the redder the auroral emissions. Hence, the ratio of green and red auroral intensity can be used to infer changes in the precipitation energy.

This study aims to measure the brightness of PMAFs and dayside aurora in the green and red channels. As PMAFs are considered to be the ionospheric signature of FTEs, they are expected to be greener than other dayside auroral forms, since particles transferred into the magnetosphere by FTEs have comparatively high energies (see sections 2.6.2 and 2.7.3). Furthermore, the dependency of auroral colour on magnetic local time is investigated, as local time heavily influences the precipitation source regions, which in turn determine the precipitation energies. For this study, the 18 PMAFs that occurred on the 18th of December 2017 (event list 2) between $6-10$ UT ($9-13$ MLT) are analysed.

A SPEA was conducted to determine the change in auroral brightness (and colour) associated with PMAF occurrence. Auroral brightness measurements were conducted using the MSP. Each scan taken by the MSP is considered separately, where the brightness is determined by a sum over all scan angles more than 20° from the horizon (20° to 160°). These bounds were chosen according to the PMAFs' highest and lowest scan angles. As the MSP data analysed in this study is not calibrated, no absolute measurement of precipitation energy was conducted, but the relative colour of PMAFs and dayside aurora is measured.

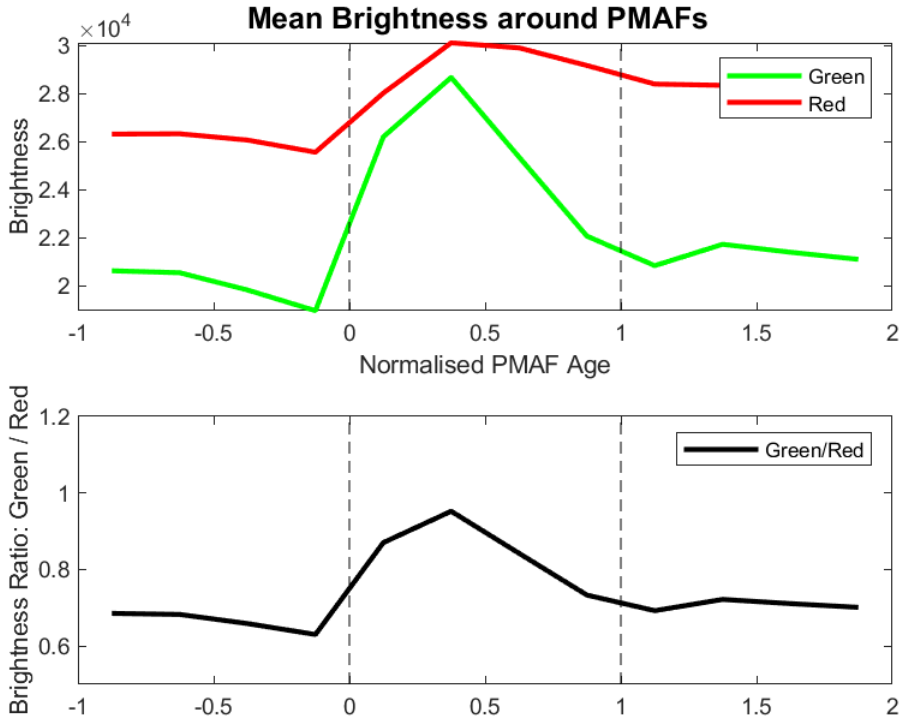

Figure 5.4: Green and red channel brightness and their ratio around PMAF events.

Figure 5.4 shows the result of the SPEA of auroral brightness in the green and red channels (upper plot). As expected, auroral brightness in the red channel is greater than in the green channel outside the PMAF life time, implying that dayside aurora is dominated by the red emission line. As the event starts, the brightness in both channels increases towards a maximum, before it approaches a slightly higher level than before the event. However, the increase in brightness is much more significant in the green channel (∼50%) than in the red channel (∼15%). This difference is even more apparent in the ratio of the two curves (lower plot).

The enhancements in the auroral brightness ratio can be attributed to the individual PMAF events by considering the ratio of the green and red channels in a keogram. Figure 5.5 shows the keograms for the 18th of December 2018 in the green and red

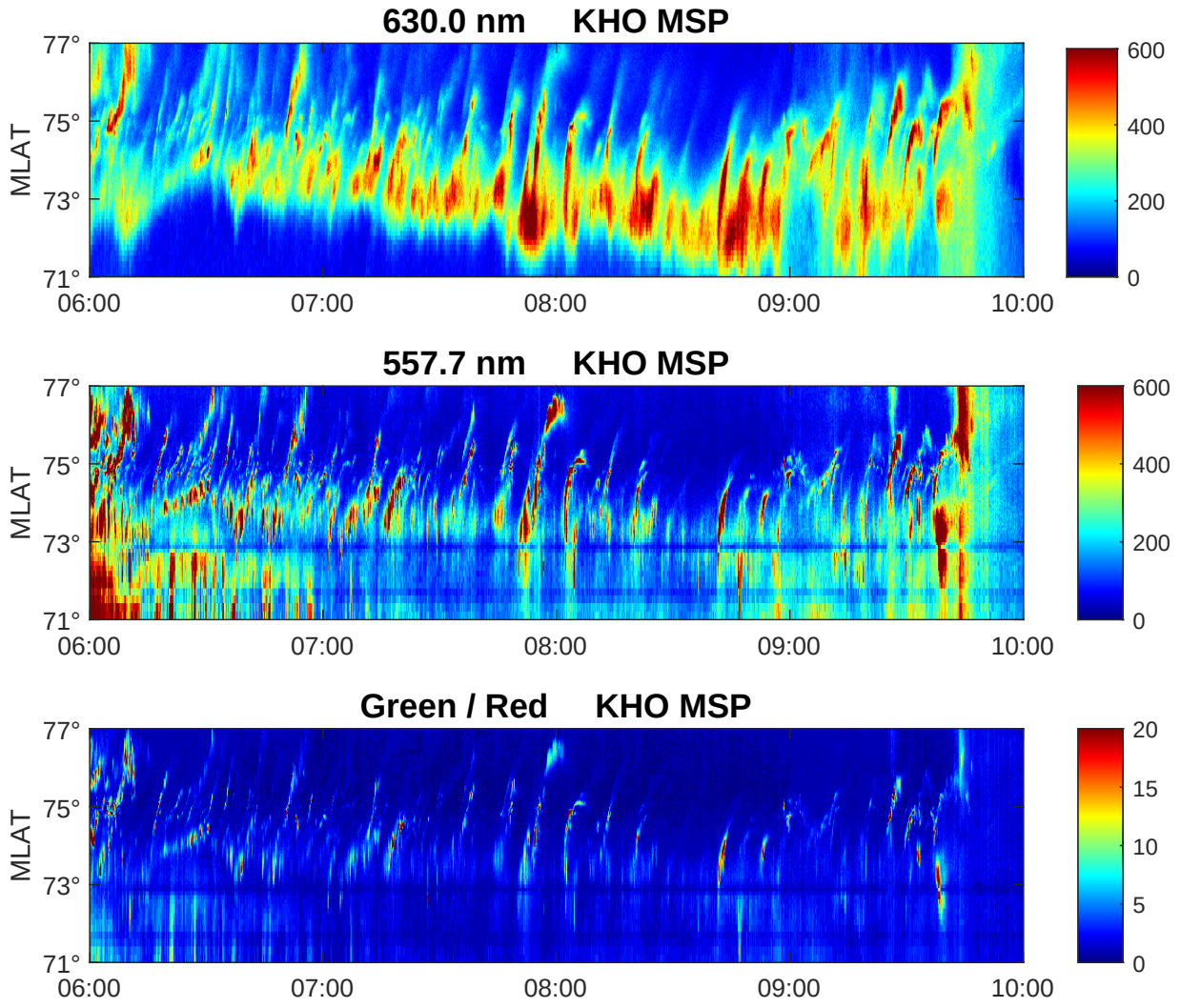

Figure 5.5: Keogram of 18.12.2017 including the green and red channels, as well as their ratio.

emission line (upper and middle panel, respectively), while their ratio is shown in the lower tile. From approximately 06:15 to 09:45 UT, cascading PMAF events can be clearly seen emerging from the auroral oval to move poleward. In many cases, EBIs and slight equatorward expansions of the auroral oval can be observed. In the auroral brightness ratio (lower panel), however, the auroral oval is barely visible. This is due to the dayside auroral oval being dominated by the red emission line. Instead, what is

most apparent is not the auroral oval, but PMAF events, as they have high green-to-red brightness ratios. This further confirms the high precipitation energies that give rise to PMAFs.

The green-to-red brightness ratio is very useful as a proxy for precipitation energy. However, it has to be mentioned, that considering the simplicity of the manner in which the channel brightness was calculated, it is difficult to distinguish between PMAF brightness (and colour) and brightness of the auroral oval, as the auroral oval was included in the calculation of emission strengths. The bounds that were chosen to calculate brightness (20° to 160° elevation) imply that at some times other auroral forms were included in the measurement. Primarily, this would affect the brightness values that were determined for the events occurring before 7 UT, as there are green aurorae in the south at that time that partially contributed to the measurement. In most other cases, the brightness values that were determined only include the emissions associated with the PMAF and (parts of) the auroral oval. This leads to unequal measurement errors in the different channels. While values for both red and green brightness are overestimated, due to the inclusion of other auroral forms, red brightness is overestimated to a greater degree, as dayside aurora is predominantly red.

Nevertheless, this does not invalidate the measurement of auroral green-to-red brightness ratio as a proxy for precipitation energy, as only the change in the ratio is of interest for this study. Additionally, figure 5.5 (in particular the brightness ratio keogram) enables one to confirm the results of this study qualitatively, showing clearly how PMAFs are associated with much stronger emission in the green channel than any other auroral form occurring on the dayside on the 18th of December 2017.

In brief, the auroral brightness of PMAFs in the red and green channels can be easily determined using a MSP. The colour of aurora can be inferred by the brightness ratio of both channels. PMAFs have been shown to be associated with significantly higher

intensities in the green emission line, compared to other dayside aurora. This difference in colour can be attributed to the higher energy of precipitating particles, caused by FTEs.

5.3 Interplanetary Magnetic Field and Solar Wind

Solar wind plasma in the magnetosheath can enter the magnetosphere through dayside reconnection, for example in a FTE. At which time and location reconnection occurs is determined by the geometry of the IMF. Thus, the properties of solar wind plasma and the IMF determine FTE, and by extension, PMAF occurrence.

This analysis covers the GSM components of the IMF and solar wind pressure, temperature and speed. In order to determine whether and how these parameters are related to PMAF occurrence, two approaches are employed. The first approach considers what values the parameters describing the IMF and solar wind have during PMAF events compared to a baseline. This baseline is chosen to be all days on which PMAFs in this dataset occurred excluding the PMAF times, similar to how the baseline was determined in the arciness study. The baseline is chosen in this manner in order for it to have the same biases, based on seasonal and solar cycle variations, as the events. Hence, any difference observed in the values of the analysed parameters between the baseline and the events can be attributed to correlations between the events and these parameters. The second approach employs SPEAs to investigate any possibilities of cause and effect relationships between the short term evolution of the analysed parameters and the occurrence of PMAF events. This approach is very useful in detecting changes in the IMF that are relevant for reconnection, where the evolution of the parameters in question are arguably more relevant than their values.

Figure 5.6 shows probability density distributions for the values of the parameters analysed in this study. The baseline is shown in blue, while the data measured during PMAF events are shown in orange. Since the baseline contains many more data points than the PMAF events, statistical fluctuations within the PMAF probability distribution are much larger. As the analysed dataset (event list 1) includes merely 23 events,

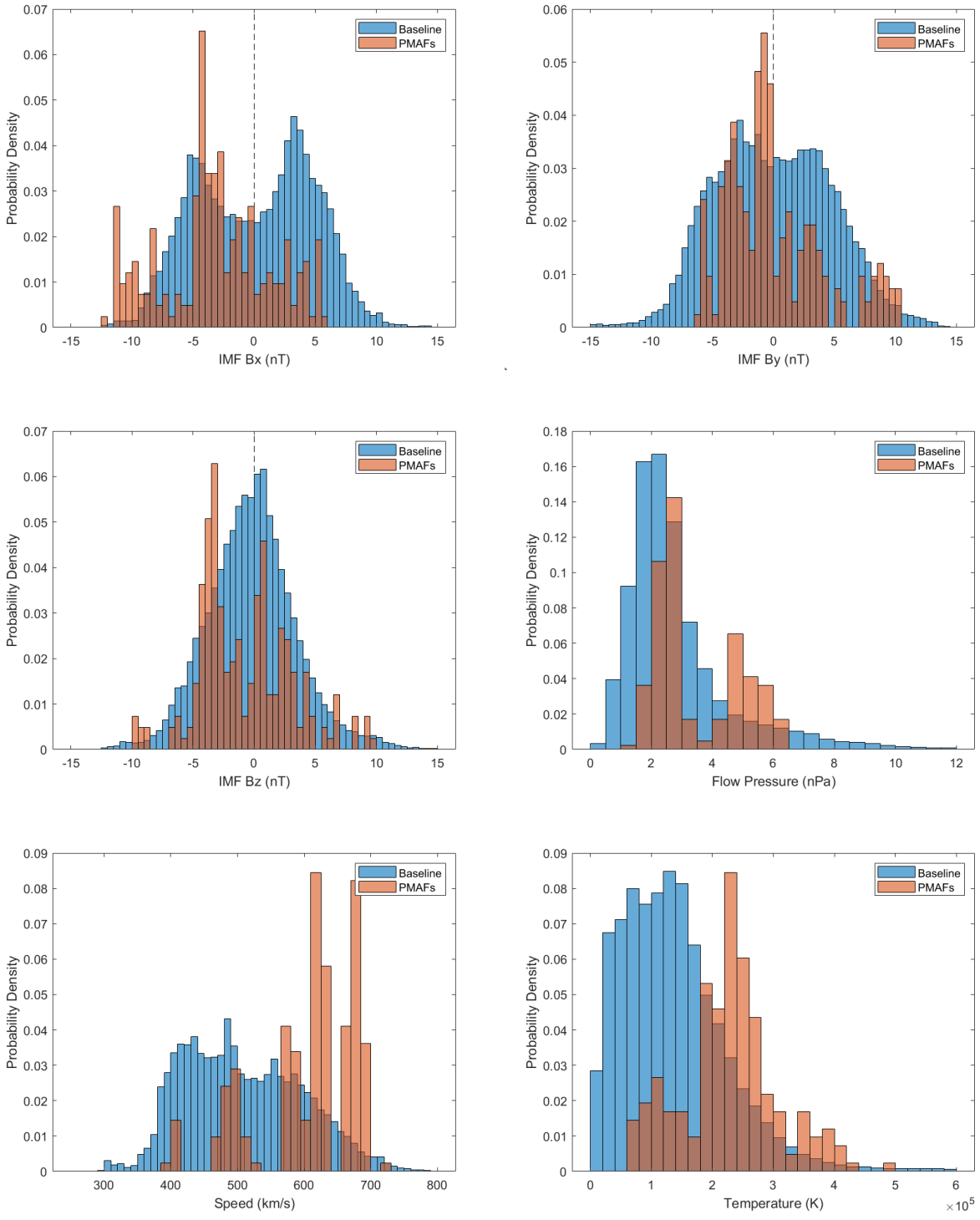

Figure 5.6: IMF and Solar wind conditions during event list 1 PMAFs (red) and their baseline (blue).

the values for each parameter within the event time frames are not averaged for each event, however instead, all values of the parameters during the events are analysed and contribute to the probability distribution. The average event duration in the first event list is approximately 6 minutes, which, when considering that IMF and solar wind data are 1 minute resolution, implies that this increases the number of data points by a factor of 6.

The plot in the upper left tile of figure 5.6 shows the distributions of IMF Bx for the events and baseline. The two distributions are not identical, which implies there is a non-zero correlation between PMAF occurrence and IMF Bx, in so far as the differences in the distributions are not due to statistical fluctuations. In particular, the average value Bx assumes in the baseline is approximately zero, while the average Bx value during PMAF events is -2.74 nT (see table 5.1), implying PMAFs are more likely to occur during $\mathrm{Bx} < 0$. Furthermore, very negative values of Bx ($< -10\,\mathrm{nT}$) seem to occur reasonably frequently during PMAF events ($\sim$10%), while they are extraordinarily rarely observed in the baseline ($\sim$1%). This would imply a 10-fold higher PMAF occurrence rate for extremely low values of Bx. It is very possible, that this observed high occurrence rate is due to statistical fluctuations, as the event list consists of only 23 PMAFs. Because, even though the number of data points is inflated by considering all data taken during the events instead of averaging all data for each event, the values of the parameters within the same event are still highly correlated. On the other hand, the observed high occurrence rate for low values of Bx does not have be due to statistical fluctuation. As, if it was merely a statistical fluctuation and PMAFs weren't any more likely to occur during low values of Bx, it would be highly unlikely that any given PMAF would occur in the extremes of the Bx distribution.

Xing et al. (2012) found PMAFs were more likely to occur for low values of Bx, as it was reported that approximately 47% of their events occurred during $\mathrm{Bx} < -1\,\mathrm{nT}$,

	Bx (nT)	**By (nT)**	**Bz (nT)**	**P (nPa)**	**T (10^5 K)**	**v (km/s)**
μ_{Baseline}	0.13	-0.07	-0.08	2.90	1.37	507
σ_{Baseline}	4.82	4.96	4.01	2.04	0.89	88.1
μ_{PMAF}	-2.74	1.56	-0.80	3.44	2.29	614
σ_{PMAF}	4.43	4.04	3.79	1.37	0.80	73.6

Table 5.1: Table showing averages (μ) and standard deviations (σ) of GSM IMF components and solar wind dynamic pressure P, Temperature T and speed v, for PMAF events and their baseline.

compared to 38% occurring at Bx > 1 nT. While the dataset analysed in this study follows the same trend, the asymmetry is larger with 69% of events occurring during Bx < -1 nT and just 20% occurring for Bx > 1 nT. This difference in the extent of the asymmetry is likely to be at least in part due to statistical fluctuation, as Xing et al. analysed roughly twenty times the number of PMAFs in this study.

The IMF By component (upper right plot in figure 5.6) is on average slightly positive during PMAF events (1.56 nT), while the average value in the baseline is zero. Interestingly enough, in this dataset there are more negative values recorded (61%) than positives, since most values are only slightly negative. In comparison, Xing et al found 60% of PMAFs to occur during eastward (By > 0) IMF, while Fasel (1995) found 77% of PMAFs to coincide with By>0. Another study, Drury et al. (2003) determined that 81% of southern hemisphere PMAFs occur during westward IMF (By < 0) . The agreement of Xing et al., Fasel and Drury et al., combined with the fact that this study found the mean of By to be positive, makes it almost certain that the observed difference in the number of positive By events is due to statistical fluctuation.

Based on the distribution of IMF Bz values (middle left plot, fig. 5.6), it seems probable that PMAFs are more likely to occur during southward IMF. This is expected, as it facilitates dayside reconnection giving rise to FTEs. Yet, a considerable amount

of PMAFs occur during northward IMF (41%), confirming all previous studies on this matter (Xing et al., Fasel and Drury with 41%, 39% and 39%, respectively). PMAFs occurring during northward IMF are likely associated with lobe reconnection, especially those with high values of By.

Moreover, it has been suggested that solar wind pressure pulses could lead to the formation of PMAFs, rather than FTEs. This would imply, that typical values for solar wind dynamic pressure during PMAF events are higher than the baseline values. As seen in figure 5.6, this is true, PMAFs do tend to occur during slightly higher values of solar wind dynamic pressure. In this dataset, the average PMAF occurs at solar wind flow pressure, that is higher than approximately 77% of the baseline. However, just based on the probability density distribution, it is impossible to determine whether PMAFs are caused by solar wind dynamic pressure pulses, or whether they are more likely to occur during high but stagnant solar wind dynamic pressure. The results of the SPEA will shed more light on this matter.

The biggest differences between the PMAF and baseline distributions are to be observed in the solar wind speeds. The average PMAF solar wind speed (614 km/s) lies at the 87th percentile of the baseline. Fasel (1995) presented the only published statistical study of solar wind speed of PMAF events to date. In this study, Fasel distinguished between so called PMAF1, PMAF2 and PMAF3 events. This classification system was based on optical properties that have to do with re-brightening of auroral emissions. He measured PMAF1, PMAF2 and PMAF3 events to occur at solar wind speeds of 460 km/s, 490 km/s and 670 km/s, respectively. These averages were all greater than the reported baseline average of approximately 400 km/s. Thus, this study supports the findings made by Fasel, relating to PMAF events occurring at higher rates during comparatively high solar wind speeds. This could be associated with increased transport of magnetic flux in the dungey cycle, as the magnetized solar wind drives magnetospheric

(and ionospheric) convection.

The situation is very similar with the solar wind temperature. The average PMAF solar wind temperature lies at approximately the 87th percentile of the baseline. Solar wind speed and temperature are positively correlated, meaning the effect size is expected to be similar. In fact, solar wind speed and temperature in the baseline are correlated at $r^2 = 0.45$. Therefore, it is not immediately apparent, if enhanced solar wind speed or temperature (or both) lead to higher PMAF frequencies. Which one of these possibilities is most likely could be investigated by controlling for one of the parameters, and re-examining the probability distribution of the other parameter. Unfortunately, this is not feasible with the small number of events analysed in this study. As it is unclear, which of these parameters are responsible for enhanced PMAF formation, all of them are considered.

While there is a lot that can be learned about the dynamics of PMAF occurrence from histograms of IMF and solar wind parameters, they do not address the temporal evolution of these parameters. IMF Bz, as the main parameter describing reconnection, is believed to strongly influence the formation of FTEs. This is especially true during southward turnings of the IMF, when Bz drops below zero, making reconnection more likely, which can ultimately lead to the formation of a PMAF. Frequently, the solar wind dynamic pressure pulses, instead of FTEs, have been suggested to be the main driving force behind PMAF occurrence. Which one of these competing ideas is closer to the truth can be determined using SPEAs. However, when investigating the effect of the geometry of the IMF on PMAF formation, one has to consider the IMF By component of events that are to be compared. By strongly influences the dynamics of a PMAF, including its position and direction. Hence, events are divided up into two groups based on the polarity of By. As this critically decreases the number of events in event list 1, the behaviour of the GSM IMF components is only analysed for event list

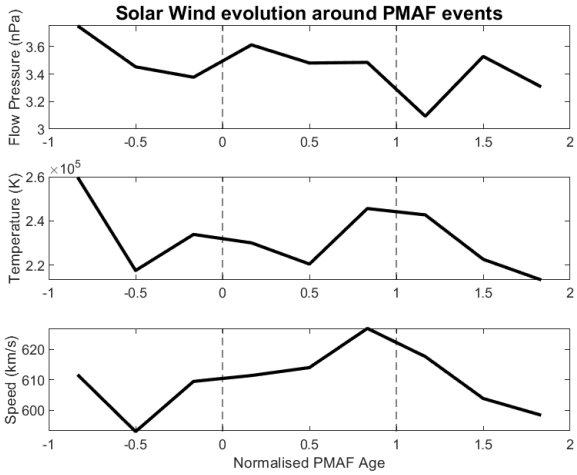

Figure 5.7: Solar wind evolution around event list 1 PMAFs.

2, as By was steadily positive during those events.

Figure 5.7 shows the results of the SPEA conducted for solar wind speed, temperature and pressure. As there is solar wind data for the first two event lists, the SPEAs are applied to both datasets separately. The results of the second event list are seen in figure 5.8. The IMF Bz component appears to show a characteristic evolution in regards to PMAF occurrence. This evolution consists of a decrease in Bz prior to the PMAF start time followed by a minimum in the middle of the event time frame. Afterwards, Bz increases again and levels off after the end of the event. The initial decrease in Bz causes the IMF to be more susceptible to reconnection, possibly leading to formation of an FTE. Wang et al (2016) conducted a similar analysis, employing SPEAs to investigate the change in Bz from 20 minutes before to 10 minutes after the start of a PMAF event. The major differences in the methodology between Wang et al and this study are that in this study, PMAF events are normalised in regards to their event time frame, and that Wang et al. considered a slightly earlier time frame relative to each event. Nevertheless, the results are very similar. Wang et al found a decrease

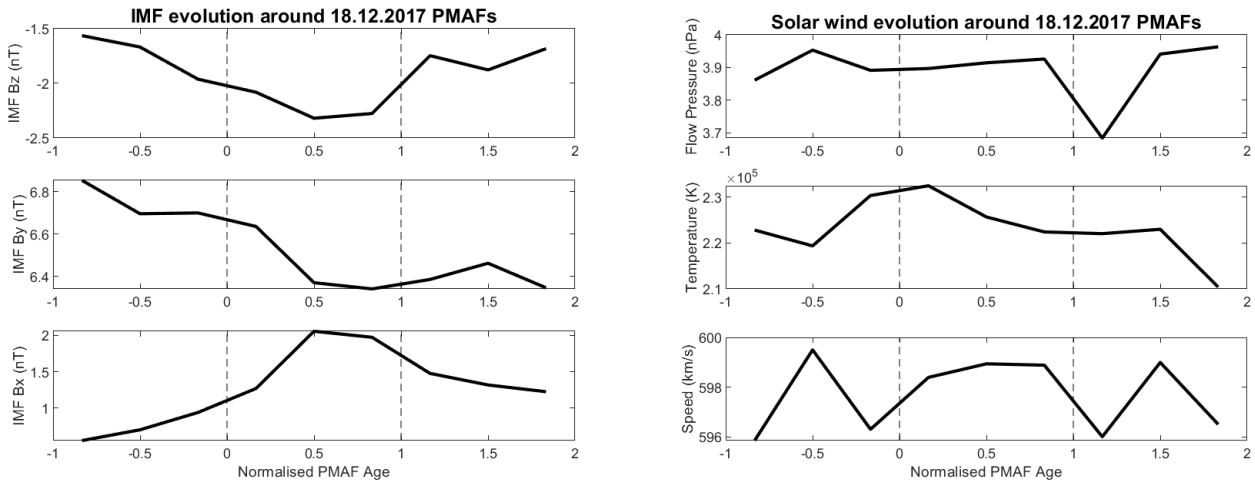

Figure 5.8: IMF and solar wind evolution around event list 2 PMAFs.

in Bz starting from roughly 5 minutes before the PMAF lifetime, which approximates to 0.5 to 1 PMAF lifetimes, on average. This lines up well with the results of the second event list. After the minimum in Bz, which was observed in both this analysis and the study by Wang et al., Bz increases again before settling at a value slightly less than Bz had before the initial drop triggering the PMAF.

Furthermore, Wang et al found that By turnings do not seem to affect PMAF occurrence. Perhaps even on the contrary, steady By is in fact associated with pulsed flows in the cusp region indicating pulsed reconnection [Moen, 2012]. This suggest that steady By might facilitate PMAF occurrence. This does seem to be what is observed in event list 2. PMAFs in the second event list occur during steady IMF By, which might contribute to the extraordinarily long time period over which PMAFs occur on that day.

The IMF Bx component does seem to show a significant change relating to PMAF occurrence. Bx increases steadily towards the end of the auroral event, at which point the value of Bx settles. While the value of Bx does play a role for PMAFs, where both negative values of Bx and high values of |Bx| increase their occurrence rate [Xing, 2012],

it is unclear how changes in Bx could affect this rate. Even though Bz and By control dayside and lobe reconnection, respectively, Bx does affect the location where reconnection occurs in the dayside magnetopause [Hoilijoki, 2014].

Pulses in the solar wind dynamic pressure have been suggested to be responsible for PMAF creation. Solar wind dynamic pressure (labelled flow pressure in figures 5.7 and 5.8) does not change significantly around PMAF events, but seems to be stagnant. Even though high values of solar wind dynamic pressure seem to facilitate PMAF occurrence, as discussed previously in this section, pressure pulses are not responsible for the formation of PMAFs in either dataset. The situation is very similar for solar wind speed and temperature. While enhanced values of solar wind speed and temperature have been found to coincide with PMAF occurrence, they are largely steady on the scale of three PMAF event time frames ($\sim$20 minutes). Hence, solar wind conditions do not correlate with PMAF occurrence on small time scales.

In summary, PMAFs are more likely to occur during southward (Bz < 0), eastward (By > 0) and sunward IMF (Bx > 0). Nevertheless, there is a large minority of PMAFs forming during northward (Bz > 0), westward (By < 0) and earthward IMF (Bx < 0). While there is a positive correlation between IMF Bz and PMAF occurrence, the change in Bz, the evolution it goes through (southward turning of the IMF) seems to be more relevant. On average, PMAFs form following a southward turning of the IMF approximately 5 minutes prior to the start of the event.

PMAFs (in these datasets) are not triggered by solar wind pressure pulses, or any other short term enhancements in solar wind temperature or speed, as all parameters describing the solar wind that were analysed were steady around PMAF event times. However, there was a significantly higher PMAF formation rate observed during high solar wind dynamic pressure, temperature and speed. This increased occurrence rate was most strongly correlated with solar wind speed and temperature.

5.4 Velocity of PMAFs and Convection

PMAFs are characterized by their poleward motion after emerging from the dayside auroral oval. The velocity of that poleward propagation has never been accurately measured. For this study, an algorithm was developed to detect the path that PMAFs take in the polar ionosphere based on their optical emissions as measured by a MSP (see section 4.3). The inherent assumption of this algorithm is that PMAFs move poleward at a constant speed, which manifests itself as a linear path in keograms. According to Fasel (1995), this assumption of constant speed is valid for more than 99% of PMAFs. The velocity of each PMAF can thus be extracted from its calculated path as it corresponds to the slope of the path. It should be noted, however, that since this algorithm uses MSP data to determine PMAF speed, it can only measure the speed along the magnetic meridian, due to the limited field of view of the MSP. Since PMAFs mainly propagate along the magnetic meridian, this remains a good measure of PMAF velocity. In fact, this algorithm delivers an upper bound for the velocity of each PMAF. In reality, PMAF speed can have a longitudinal component, which is strongly influenced by IMF By [Xing, 2012, Frey, 2019].

Figure 5.9 shows a histogram of the velocities of all PMAFs in event list 2 as determined by the algorithm. The mean velocity is approximately $\bar{v} = 960\,\mathrm{m/s}$ with a standard deviation of $\sigma_v = 350\,\mathrm{m/s}$. All measured velocities fall within a range from $400\,\mathrm{m/s}$ to $1750\,\mathrm{m/s}$ in an approximately bell-shaped distribution. While there have not been accurate measurements of PMAF velocities in the past, Oksavik et al. (2005) estimated the speed of a single PMAF to be $500\,\mathrm{m/s}$ based on ASC and EISCAT Svalbard Radar (ESR) data. This estimate is in good agreement with the measurements presented in this study, coming in at approximately one standard deviation below the mean of this dataset.

Moreover, the estimate by Oksavik at al. was in line with ionospheric convection speeds,

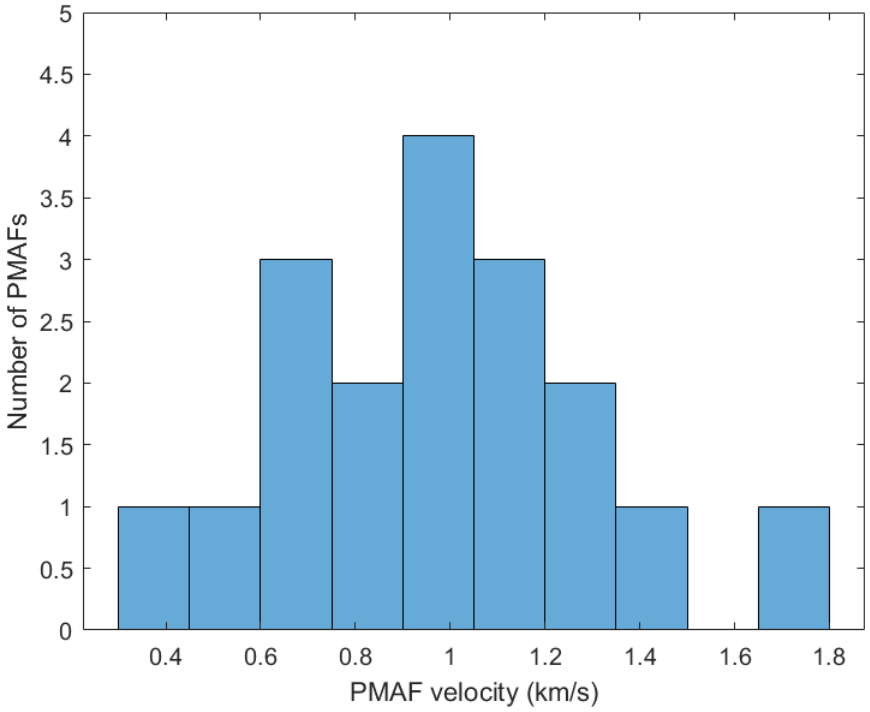

Figure 5.9: Histogram of event list 2 velocities, with a mean of $\bar{v} = 960\,\mathrm{m/s}$ and a standard deviation of $\sigma_v = 350\,\mathrm{m/s}$.

suggesting PMAFs move within the large scale flow patterns. This is thought to be a common feature of some types of dayside auroral forms [Frey, 2019]. In particular, diffuse aurora in the equatorward portion of the dayside auroral oval can show small scale (10s of km) structures, such as patches, stripes and bands, that move along with the large scale convection [Han, 2015, Ebihara, 2007]. However, there are some dayside auroral forms that can drift at significantly higher speeds than PMAFs and small scale structures embedded within diffuse aurora. For instance, Motoba et al. (2017) found auroral patches moving at $\sim 20\,\mathrm{km/s}$, significantly exceeding convection speeds.

However, it needs to be emphasized, that typical velocities of PMAFs ($\sim 1\,\mathrm{km/s}$) are higher than average polar convection speeds ($\sim 500\,\mathrm{m/s}$). Though, this does not indicate that PMAFs do not move within the global ionospheric convection pattern. Instead,

it has been suggested, PMAFs do preferentially occur during times of enhanced ionospheric flow, in so called flow channel events (FCEs) [Neudegg, 2001, Thorolfsson, 2000].

5.4.1 Flow Channels

FCEs are the ionospheric signature of FTEs as observed by HF radars, hence they are inherently and closely related to PMAFs. They manifest themselves as latitudinally narrow (< 100 km) and longitudinally wide (> 1000 km) structures of enhanced flow in the F region of the ionosphere [Pinnock, 1993, Goertz, 1985, Eyken, 1984]. Frequently, FCEs are also referred to as poleward moving radar auroral forms (PMRAFs), convection channels, bursts or pulsed ionospheric flows, depending on the mechanism through which a specific event is found. However, these phenomena are inherently related and only differ in particular characteristics [Wild, 2001, Davies, 2000].

The aim of this study was to measure flow channel events occurring together with PMAFs that were identified using optical data. This allows testing our understanding of the small scale dynamic current system (see section 2.7.3) that forms during PMAF activity. Furthermore, the velocity of PMAFs can be compared to the line-of-sight ion velocity as measured by SuperDARN.

This study uses event list 3, which is the only dataset in this thesis that has SuperDARN, MSP and IMF data available for each event, allowing comparison between optical and radar signatures of FTEs. It includes nine events occurring in succession in a less than an hour. The keogram for the red and green auroral emission line is plotted in figure 5.10, along with the line-of-sight ion velocity and the GSM IMF components. The algorithm calculating the PMAF path and velocity has been applied to these events as well. The path of each event is drawn into the keograms and the SuperDARN data as a black line.

The geometry of the IMF was very conducive to PMAF formation, which likely con-

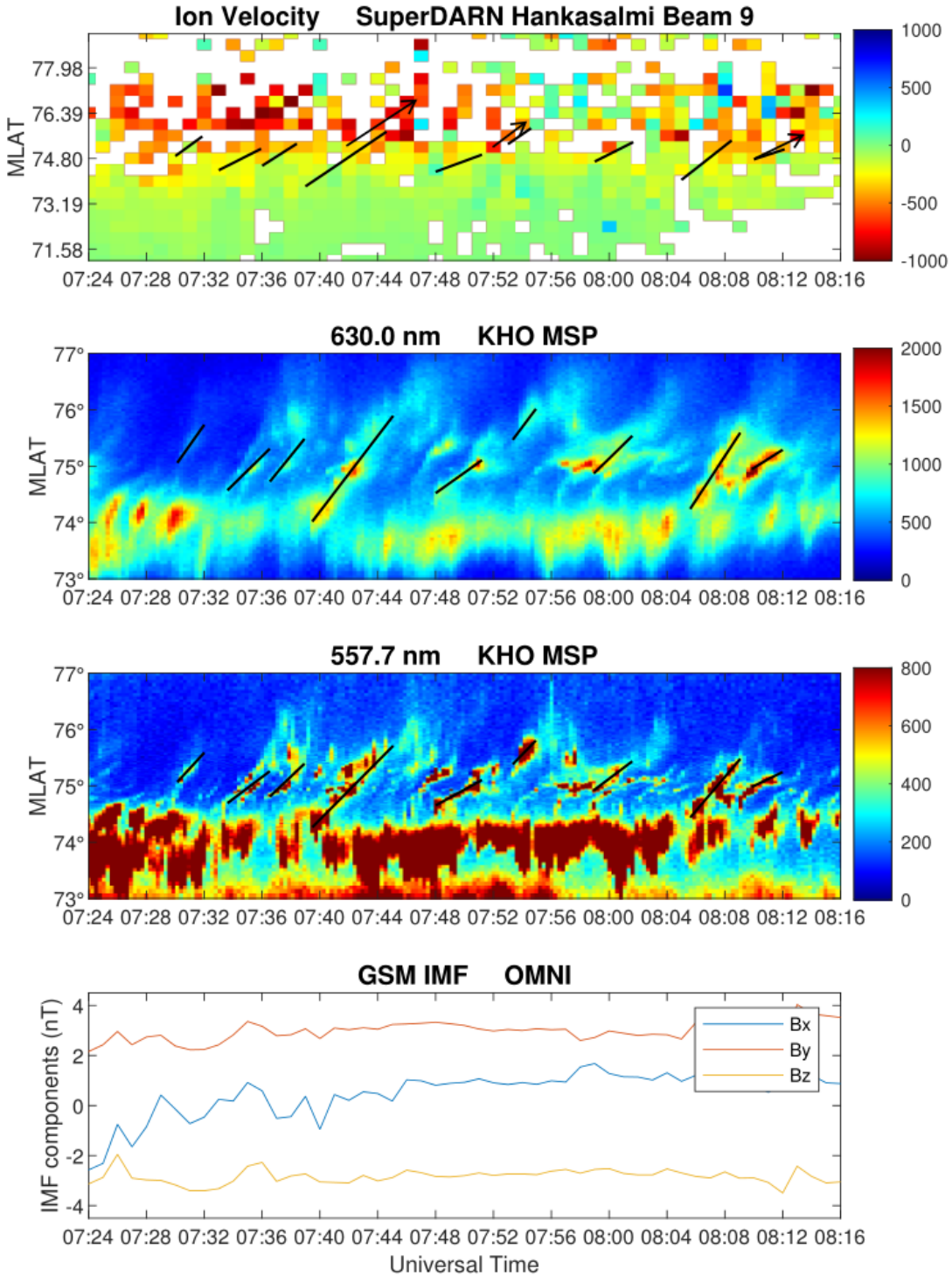

Figure 5.10: Overview plot of 10th of December 2013 PMAF events including Hankasalmi ion velocity data (top), keograms in the red and green channels (middle) and values of IMF components (bottom).

tributed to the large number of cascading PMAFs that were observed during this event period. Bz was consistently negative at around −3 nT, enabling dayside reconnection (see sections 2.5 and 5.3). IMF By was positive, which has been found to be associated with a higher PMAF formation rate (in this thesis and by Xing et al. (2012)). Furthermore, By was very steady, which is associated with pulsed reconnection [Moen, 2012]. From the keogram, it can be estimated, that the auroral oval was situated at approximately 74° MLAT. The PMAFs emerged from the oval to propagate poleward before fading at around 76° MLAT, having travelled a little over 200 km. Most of the events had comparatively small lifetimes, on average about 3.5 minutes. This implies, their radar signature likely only spans three to four time bins (due to the 1 minute SuperDARN resolution) and also three to four range gates (each range gate has a width of 45 km) that are aligned diagonally from the lower left to the top right, very similar to the way PMAFs manifest themselves in keograms.

However, considering the limitations SuperDARN data has (see section 3.4), especially geolocation uncertainties, and spatial and temporal resolution limitations, it is practically impossible to map a single optical event to a radar signature with confidence. In many cases it may seem plausible (or even likely), that a given structure in the SuperDARN data corresponds to particular optical event. These flow structures are marked with a black arrow in figure 5.10. For example, the optical event starting at 07:39 UT is potentially related to the patch of fast moving plasma occurring near the end of the optical event. And similarly, the PMAFs starting at 07:53 UT and 08:10 UT occur within structures of enhanced ion velocity that are surrounded by regions of lower velocity or without any backscatter. These two structures in particular are likely flow channel events associated with each PMAF, however, no definitive statement can be made given the uncertainties of the data.

These limitations, implying no one-to-one correspondence between optical and radar

event can be made, also prevent any meaningful quantitative comparison between the PMAF velocity as determined by the algorithm and the line-of-sight ion velocity as measured by SuperDARN. But, qualitatively, all PMAFs in this dataset occur within or close to patches of enhanced poleward ion velocity. During the first six events, from 07:28 UT to 07:53 UT, there is typically little to no time between the end of one event and the start of the next. In this time frame, many enhanced poleward flows can be observed north of 75° MLAT, where most of the optical events start, with very little backscatter showing equatorward or net zero flow. After 07:53 UT, no successive event starts until 07:59 UT. During this time, the Hankasalmi radar measured most of the flow north of 75° MLAT to be equatorward or net zero, without any structures of (enhanced) poleward flow.

The situation is similar until 08:05 UT, when most flow seems to be poleward again and two more PMAFs occur. This indicates, that the structures of enhanced poleward flow are closely related to the optical events, as the occurrence of both phenomena seem to be correlated for the duration of these cascading events.

There are a few instances, in which there is equatorward flow detected by SuperDARN in the vicinity of PMAFs, as for example at 07:47 UT, 07:54 UT and 08:06 UT. Frequently, these reverse flows occur poleward of the regions of enhanced poleward flow. However, considering the geolocation uncertainties and the fact, that these equatorward flows are observed in a very small number of range gates, it is difficult to identify them as the return flow associated with the current system.

Thus, PMAFs (in this study) seem to occur in regions of enhanced ion velocity, which can be understood based on the formation of a flow channel as part of a dynamic current system coupling the magnetosphere to the polar ionosphere. These observations are consistent with the description of ionospheric FTE signatures by Southwood (1987), which predicted the existence of a central anti-sunward (poleward) flow.

There have been a few similar studies so far. McWilliams et al. 2004 investigated the location of FTEs and their ionospheric signatures using satellite and ground based data. The study detected a large number of FTE signatures using six different radars that are all part of the SuperDARN network, including the Hankasalmi radar. The observed signatures manifested themselves as small structures of enhanced poleward flow ($<\sim 1\,\mathrm{km/s}$) with lifetimes of a few minutes, very closely resembling the structures observed in this study. This further supports the interpretation of the structures observed in this study as FCEs related to PMAFs.

Oksavik et al. (2004) studied a PMAF occurring east of Svalbard and measured parts of the flow pattern associated with the event using the EISCAT Svalbard Radar (ESR). The main differences between this study and the study carried out by Oksavik et al. are firstly, the different spatial resolutions that SuperDARN and the ESR operate at. The ESR has a finer spatial resolution allowing identification of small scale structures and mapping them to optical events, which turns out to be impractical with SuperDARN, in the case of PMAFs. And secondly, different parts of the PMAF current system were measured by Oksavik et al. and in this study. Since the observed event occurred east of Svalbard, where the ESR is located, Oksavik et al. measured the east-west component of the flow system, as only the line-of-sight component can be measured. The findings of the study point to the presence of an upward Birkeland current filament and small scale flow distortion as part of a localized dynamic current system. This current system was only observed within the seven minute time frame of the optical event, implying their relation. The observations made by Oksavik et al. suggest the current system is consistent with the FTE model first proposed by Southwood (1985).

6 Conclusions and Outlook

This thesis consists of four distinct studies addressing the morphology and dynamics of poleward moving auroral forms. In the first part of the thesis, the behaviour of the arciness index in relation to PMAF activity is investigated. While arciness values during PMAF activity are generally higher than during the rest of the dayside, this effect is relatively minor, as there is much more overlap than difference. Yet, a superposed epoch analysis uncovered a characteristic evolution the arciness value exhibits over the course of a PMAF event, in which arciness increases due to the formation of a PMAF and subsequently decays back to its original value as the PMAF propagates poleward and fades over time. This relationship between arciness and PMAF occurrence has been found to hold true regardless of the manner in which arciness is calculated and the ASC images are taken in. These findings pave the way for the development of an automated PMAF detection algorithm based on arciness. Automatic PMAF detection based on optical data has been found to be extremely difficult, which makes the possibility of an arciness-based detection algorithm very promising.

The second part of the thesis covered the brightness of PMAFs in the red and green auroral emission lines. PMAFs were shown to be associated with significantly higher intensities in the green emission line compared to other dayside aurora. Furthermore, the ratio of brightness in the green and red channels is used as a proxy for precipitation energy, demonstrating, that PMAFs are caused by higher energy precipitation than other dayside auroral forms. This enhanced precipitation energy is associated with the processes causing plasma heating and acceleration during magnetic reconnection, sup-

porting the notion that the observed PMAFs are the ionospheric signatures of FTEs. Thirdly, the influence of the geometry and strength of the interplanetary magnetic field as well as the properties of the solar wind on PMAF formation rates were investigated. PMAFs have been found to form more frequently during southward (Bz<0), eastward (By>0) and sunward (Bx>0) IMF, confirming previous studies on this matter. Nevertheless, it must be mentioned, that there is a large minority of PMAFs occurring during unfavourable IMF conditions. This study also showed, there is a characteristic decrease in IMF Bz prior to the start of a PMAF, which is likely conducive to pulsed dayside reconnection. Moreover, short term enhancements in solar wind temperature, speed and dynamic pressure do not trigger PMAFs, ruling out solar wind dynamic pressure pulses as a competing theory for FTEs as a trigger mechanism for PMAFs in this dataset. Nevertheless, solar wind properties affect PMAF activity. In particular, enhanced solar wind speed and temperature are associated with high PMAF formation rates. Future studies could attempt to replicate this influence, that enhanced solar wind activity appears to have on PMAF formation, given that this study had a comparatively small sample size.

Lastly, a newly developed algorithm that measures the position and velocity of PMAFs was applied to 18 events. These events had poleward propagation speeds of approximately 1 km/s with a standard deviation of 360 m/s. However, it is unclear what the determining factors of this velocity are. It would be worth investigating if typical PMAF speeds depend on the conditions of the solar wind and IMF, and if they are related to other metrics such as local time, lifetime, brightness, precipitation energy, etc.

Another nine PMAF events were observed using optical (MSP) and radar (SuperDARN) instruments. It could be demonstrated, that the optical events occur within localized regions of enhanced ionospheric flow, which are thought to be part of a small

scale dynamic current system, as described by Southwood. Possibly, other parts of this current system including equatorward return flow could be observed. In the future, larger datasets could be used to test whether the measured positions of optical events agree with the locations of flow channels statistically. This would determine if individual PMAFs could be mapped to FCEs using SuperDARN data. There is great possibility in using SuperDARN data for this purpose, due to the near continuous data coverage that SuperDARN offers, as well as the considerably large field of view in both hemispheres. Moreover, it would be worth studying the same event using radars at different locations, enabling the measurement of different parts of the same current system associated with a single PMAF.

7 Acknowledgements

First and foremost, I want to say how hugely grateful I am to my main supervisor, Lisa Baddeley. Lisa, you made it possible for me to come to Svalbard, this amazing place that feels like home to me now, and for showing me the world of space physics. It always felt like, whenever I was stuck on a problem for a while and asked you for help, you made it a point to immediately work on a solution and wouldn't stop until you found one. And in my writing phase you somehow read my drafts within just a few days and came back with detailed and helpful comments. Thank you very much for your supervision, advice and encouragement!

This project simply wouldn't have been the same, or as much fun, without you, Noora. I'm extremely grateful to have had you as my co-supervisor. It is astounding that I could run into you in the hall and talk with you for two hours without noticing time passing. To this day, I'm still amazed by how quickly you would come up with suggestions, helpful comments and would give encouragement whenever I shared preliminary results. On a somewhat unrelated note, I'm also amazed by how fast and seamlessly you can climb the masts of the SuperDARN interferometer array!
I look forward to working with you and Lisa on publishing the results of my thesis and I hope our collaboration has just begun!

René, I want to thank you very much for not just examining my thesis, but for welcoming me into your group. It has been invaluable for me to have the opportunity to regularly present my results to a scientific audience outside space physics. It also taught me to

speak about my work in German, which I think shouldn't have been as difficult as it was. And after I returned from Svalbard, you even provided me with my own office! I'm very happy our collaboration is also just beginning, thank you!

There is not enough space here to thank everyone that helped me in some way by name. But, I do want to say thank you to Emma Bland for all the guidance with SuperDARN. Thank you to Katie Herlingshaw for all the helpful hints interesting conversations. I'm very glad to have met you, Mikko Syrjäsuo, thank you for teaching me a lot about field safety and operations and letting me participate in the construction of SuperDARN's interferometer array! Thanks to Kjersti Kalhagen for the nice company during not so conventional work hours. And thank you to the entire AGF department at UNIS for being such a fun and knowledgable group of people!

Lastly, I want to thank my fellow students. You put the cherry on top of my year in Svalbard, by accompanying me on snowmobile trips at literally any time of day, sharing the rifle carrying duties on out of town runs, building igloos and exploring ice caves with me, tolerating my highmarking no matter how overloaded the sledge I was pulling was, and being wonderful company to eat, work, study, complain, gossip, watch football and formula 1, knit (!), dance, hike, mountaineer, ski, and of course, scooter with. Takk for turen!

References

[Baumjohann and Treumann, 2012] Baumjohann, W. and Treumann, R. (2012). *Basic Space Plasma Physics - Revised Edition*. Imperial College Press.

[Bertaux, 2005] Bertaux, J. (2005). Discovery of an aurora on mars. *Nature*.

[Bhardwaj, 2012] Bhardwaj, A. (2012). Coupled chemistry-emission model for atomic oxygen green and red-doublet emissions in comet c/1996 b2 hyakutake. *The Astrophysical Journal*.

[Brekke, 2013] Brekke, A. (2013). *Physics of the Upper Polar Atmosphere*. Springer Atmospheric Sciences.

[Cogger, 1977] Cogger (1977). Characteristics of dayside 557.7 nm and and 391.4 nm aurora. *Geophysical Research Letters*.

[Daly, 1981] Daly, P. (1981). Particle signature of magnetic flux transfer events at the magnetopause. *Journal of Geophysical Research*.

[Dandekar, 1977] Dandekar, B. (1977). Dayside auroral gap. *American Geophysical Union*.

[Dandekar, 1978] Dandekar, B. (1978). The midday, discrete auroral gap. *Journal of Geophysical Research*.

[Davies, 2000] Davies, J. (2000). Ground-based observations of the auroral zone and polar cap ionospheric responses to dayside transient reconnection. *Ann. Geophys.*

[Drury, 2003] Drury, E. E. (2003). Southern hemisphere poleward moving auroral forms. *Journal of Geophysical Research: Space Physics*.

[Ebihara, 2007] Ebihara (2007). Quasi-stationary auroral patches observed at the south pole station. *Journal of Geophysical Research, Space Physics.*

[Eyken, 1984] Eyken, V. (1984). Initial eiscat observations of plasma convection at invariant latitudes 70-77. *Journal of Atmospheric and Terrestrial Physics.*

[Fasel, 1992] Fasel, G. (1992). Multiple brightenings of transient dayside auroral forms during oval expansions. *Geophysical Research Letters.*

[Fasel, 1995] Fasel, G. (1995). Dayside poleward moving auroral forms: A statistical study. *Journal of Geohphysical Research: Space Physics.*

[Floyd, 2002] Floyd, L. (2002). Solar uv irradiance, its variation, and its relevance to the earth. *Advances in Space Research*, 29(10):1427–1440.

[Foster, 1981] Foster, J. C. (1981). Large scale patterns of auroral ionospheric convection observed with the chatanika radar. *Journal of Geophysical Research.*

[Foster, 1986] Foster, J. C. (1986). Ionospheric convection associated with discrete levels of particle precipitation. *Geophysical Research Letters.*

[Frey, 2019] Frey, H. (2019). Dayside aurora. *Space Science Reviews.*

[Goertz, 1985] Goertz, C. (1985). Observations of a possible ground signature of flux transfer events. *Journal of Geophysical Research: Space Physics.*

[Han, 2015] Han, D. (2015). An extensive survey of dayside diffuse aurora based on optical observations at yellow river station. *Journal of Geophysical Research, Space Phyiscs.*

[Han, 2021] Han, D. (2021). The critical factor in controlling the auroral intensity in the cusp region as revealed by a statistical study on midday gap and non-gap events. *Geophysical Research Letters.*

[Heelis, 1986] Heelis, R. A. (1986). Ionospheric convection signatures observed by de 2 during northward interplanetary magnetic field. *Journal of Geophysical Research, Space Physics.*

[Hoilijoki, 2014] Hoilijoki, S. (2014). Magnetopause reconnection and energy conversion as influenced by the dipole tilt and the imf bx. *Journal of Geophysical Research: Space Phyiscs.*

[Hui, 2010] Hui, Y. (2010). What can be learned from the absence of auroral x-ray emission from saturn? *Journal of Geophysical Research Atmospheres.*

[Hwang, 2020] Hwang, K. (2020). Sequential observations of flux transfer events, poleward moving auroral forms, and polar cap patches. *Journal of Geophysical Research: Space Physics.*

[Kivelson and Russel, 1995] Kivelson and Russel (1995). *Introduction to Space Physics.* Cambridge atmospheric and space science series. Cambridge University Press.

[Laundal, 2017] Laundal, K. (2017). Magnetic coordinate systems. *Springerlink.com.*

[Lockwood, 1989] Lockwood, M. (1989). Dayside auroral activity and magnetic flux transfer from the solar wind. *Geophysical Research Letters.*

[Lorentzen, 2010] Lorentzen, D. (2010). In situ measurement of a newly created polar cap patch. *Journal of Geophysical Research: Space Physics.*

[Lundin, 1986] Lundin, M. (1986). Auroral morphology of the midday oval. *Geophysical Research Letters.*

[Mende, 2009] Mende, S. (2009). Coordinated observation of the dayside magnetospheric entry and exit of the themis satellites with ground-based auroral imaging in antarctica. *Journal of Geophysical Research: Space Physics.*

[Meng, 1988] Meng, N. (1988). The cusp and the cleft/boundarlayer: Low-altitude identification and statistical local time variation. *Journal of Geophysical Research.*

[Moen, 2012] Moen, J. (2012). Multi-scale features of solar terrestrial coupling in the cusp ionosphere. *Journal of Atmospheric and Solar-Terrestrial Physics.*

[Motoba, 2017] Motoba (2017). Fast-moving diffuse auroral patches. *Journal of Geophysical Research: Space Physics.*

[Neudegg, 1999] Neudegg, D. (1999). A flux transfer event observed at the magnetopause by the equator-s spacecraft and in the ionosphere by the cutlass hf radar. *Annales Geophysicae.*

[Neudegg, 2001] Neudegg, D. (2001). The uv aurora and ionospheric flows during flux transfer events. *Ann. Geophys.*

[Newell and Meng, 1992] Newell, P. and Meng, C. (1992). Mapping the dayside ionosphere to the magnetosphere according to particle precipitation characteristics. *Geophysical Research Letters.*

[Nishitani, 2019] Nishitani, N. (2019). Review of the accomplishments of mid-latitude super dual auroral radar network (super-darn) hf radars. *Progress in Earth and Planetary Science.*

[Nozawa, 2018] Nozawa, S. (2018). A new five-wavelength photometer operated in tromsÃž. *Earth Planets Space.*

[Oksavik, 2004] Oksavik, K. (2004). High-resolution observations of the small-scale flow pattern associatedwith a poleward moving auroral form in the cusp. *GEOPHYSICAL RESEARCH LETTERS.*

[Oksavik, 2005] Oksavik, K. (2005). Multi-instrument mapping of the small-scale flow dynamics related to a cusp auroral transient. *Annales Geophysicae*.

[Partamies, 2014] Partamies, N. (2014). Solar cycle and diurnal dependence of auroral structures. *Journal of Geophysical Research: Space Physics*.

[Pinnock, 1993] Pinnock, M. (1993). Observations of an enhanced convection channel in the cusp ionosphere. *Journal of Geophysical Research: Space Physics*.

[Rinne, 2010] Rinne, Y. (2010). Stratification of east west plasma flow channels observed in the ionospheric cusp in response to imf by polarity changes. *Geophysical Research Letters*.

[Sanchez, 1990] Sanchez, E. (1990). Observations of solar wind penetration into the earth's magnetosphere: The plasma mantle. *Johns Hopkins APL Technical Digest*.

[Sandel, 1981] Sandel, B. R. (1981). Morphology of saturn's aurora. *Nature*.

[Sandholt, 1986] Sandholt, P. (1986). Signatures in the dayside aurora of plasma transfer from the magnetosheath. *Journal of Geophysical Research: Space Physics*.

[Sibeck, 1990] Sibeck, D. (1990). A model for the transient magnetospheric response to sudden solar wind dynamic pressure variations. *Journal of Geophysical Research, Space Physics*.

[Sibeck, 1992] Sibeck, D. (1992). Transient events in the outer magnetosphere: Boundary waves or flux transfer events? *Journal of Geophysical Research: Space Physics*.

[Southwood, 1985] Southwood (1985). Theoretical aspects of ionosphere-magnetosphere-solar wind coupling. *Advanced Space Research*.

[Southwood, 1987] Southwood (1987). The ionospheric signatures of flux transfer events. *Journal of Geophysical Research*.

[SpaceWeatherLive, 2021] SpaceWeatherLive (2021). Spaceweatherlive. Weblink, SpaceWeatherLive, "https://www.spaceweatherlive.com/en/help/the-interplanetary-magnetic-field-imf.html".

[Thorolfsson, 2000] Thorolfsson, J. (2000). Simultaneous optical and radar signatures of poleward moving auroral forms. *Ann. Geophys.*

[Wang, 2016] Wang, B. (2016). Investigation of triggering of poleward moving auroral forms using satellite-imagercoordinated observations. *Journal of Geophysical Research: Space Physics.*

[Wild, 2001] Wild, J. (2001). First simultaneous observations of flux transfer events at the high-latitude magnetopause by the cluster spacecraft and pulsed radar signatures in the conjugate ionosphere by the cutlass and eiscat radars. *Ann. Geophys.*

[Xing, 2012] Xing, Z. (2012). Poleward moving auroral forms (pmafs) observed at the yellow riverstation: A statistical study of its dependence on the solar wind conditions. *Journal of Atmospheric and Solar-Terrestrial Physics.*

[Xing, 2013] Xing, Z. (2013). Dayside poleward moving auroral forms and ionospheric convection under stable interplanetary magnetic field (imf) conditions. *SCIENCE CHINA Technological Sciences.*

[Yoeman, 2001] Yoeman, T. (2001). An evaluation of range accuracy in the super dual auroral radar network over-the-horizon hf radar systems. *Radio Science.*

Eigenständigkeitserklärung

Hiermit erkläre ich, dass ich die Arbeit selbstständig und ohne Benutzung anderer als der angegebenen Quellen und Hilfsmittel verfasst habe. Alle Stellen der Arbeit, die wörtlich oder sinngemäß aus Veröffentlichungen oder aus anderen fremden Texten entnommen wurden, sind von mir als solche kenntlich gemacht worden. Ferner erkläre ich, dass die Arbeit nicht - auch nicht auszugsweise - für eine andere Prüfung verwendet wurde.

Longyearbyen, 10.08.2021 Anton Goertz